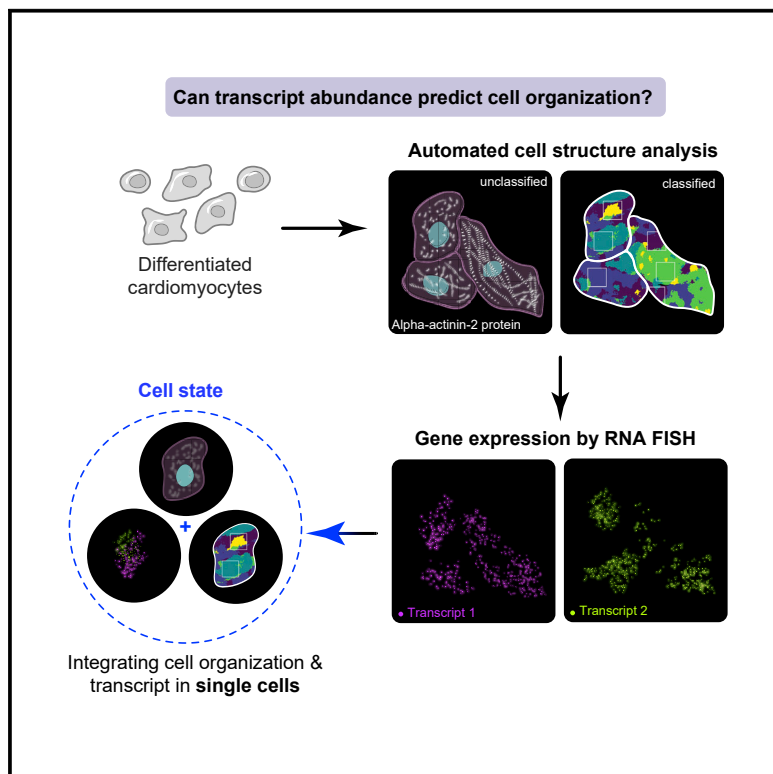


Cell states beyond transcriptomics: Integrating structural organization and gene expression in hiPSC-derived cardiomyocytes

Graphical abstract



Authors

Kaytlyn A. Gerbin, Tanya Grancharova,
Rory M. Donovan-Maiye,
Melissa C. Hendershott, ...,
Susanne M. Rafelski, Julie A. Theriot,
Ruwanthi N. Gunawardane

Correspondence

rug@alleninstitute.org

In brief

This study establishes a framework for multidimensional analysis in single cells to study the relationship between gene expression and cell organization. The quantitative and automated image analysis tools developed in the study were applied to thousands of single cells, and the results suggest that gene expression alone is not sufficient to classify cell states.

Highlights

- Automated image-based classification of subcellular organization in single cells
- Integrated analysis of gene expression and cell structure to classify cell state
- Curated dataset containing over 30,000 hiPSC-derived cardiomyocytes
- Open-source images, analysis code, and quantitative tools



Article

Cell states beyond transcriptomics: Integrating structural organization and gene expression in hiPSC-derived cardiomyocytes

Kaytlyn A. Gerbin,^{1,3} Tanya Grancharova,^{1,3} Rory M. Donovan-Maiye,^{1,3} Melissa C. Hendershott,^{1,3} Helen G. Anderson,¹ Jackson M. Brown,¹ Jianxu Chen,¹ Stephanie Q. Dinh,¹ Jamie L. Gehring,¹ Gregory R. Johnson,¹ HyeonWoo Lee,¹ Aditya Nath,¹ Angelique M. Nelson,¹ M. Filip Sluzewski,¹ Matheus P. Viana,¹ Calysta Yan,¹ Rebecca J. Zaunbrecher,¹ Kimberly R. Cordes Metzler,¹ Nathalie Gaudreault,¹ Theo A. Knijnenburg,¹ Susanne M. Rafelski,¹ Julie A. Theriot,^{1,2} and Ruwanthi N. Gunawardane^{1,4,*}

¹Allen Institute for Cell Science, 615 Westlake Ave N, Seattle, WA, USA

²Department of Biology and Howard Hughes Medical Institute, University of Washington, Seattle, WA, USA

³These authors contributed equally

⁴Lead contact

*Correspondence: rug@alleninstitute.org

<https://doi.org/10.1016/j.cels.2021.05.001>

SUMMARY

Although some cell types may be defined anatomically or by physiological function, a rigorous definition of cell state remains elusive. Here, we develop a quantitative, imaging-based platform for the systematic and automated classification of subcellular organization in single cells. We use this platform to quantify subcellular organization and gene expression in >30,000 individual human induced pluripotent stem cell-derived cardiomyocytes, producing a publicly available dataset that describes the population distributions of local and global sarcomere organization, mRNA abundance, and correlations between these traits. While the mRNA abundance of some phenotypically important genes correlates with subcellular organization (e.g., the beta-myosin heavy chain, *MYH7*), these two cellular metrics are heterogeneous and often uncorrelated, which suggests that gene expression alone is not sufficient to classify cell states. Instead, we posit that cell state should be defined by observing full distributions of quantitative, multidimensional traits in single cells that also account for space, time, and function.

INTRODUCTION

The earliest classifications of cells, developed well over a century ago, focused on their morphologies and locations in specific organs and tissues and revealed the intimate relationship between cell structure and function (Abbot, 1916; Ophüls, 1906). Subsequent studies enriched this relationship, showing the specialized intracellular organization of different cell types. For example, neurons have long projections that allow rapid transmission of electrical signals and synaptic specializations at their tips for cell-to-cell communication (Kandel et al., 2012), and muscle cells have a highly specialized contractile apparatus to permit efficient force production (Huxley and Niedergerke, 1954; Huxley and Hanson, 1954). Even within a cell type, cells can exist in a number of functional states, such as the massive cellular reorganization and formation of the mitotic spindle that occurs during mitosis (reviewed in Champion et al. 2017), the polarization accompanying cell invasion (Etienne-Manneville, 2008), or the programmed cellular destruction during apoptosis (Bottone et al., 2013). More recently, single-cell RNA sequencing (scRNA-seq) has added yet another dimension, revealing transcriptomic signatures of known and putative cell types during

development (reviewed in Ackers-Johnson et al., 2018; Cao et al., 2016; Chaudhry et al., 2019; DeLaughter et al., 2016; Kokkinopoulos et al., 2015; Lescroart et al., 2018; Li et al., 2016; Paik et al., 2020; Sereti et al., 2018; Suryawanshi et al., 2020; Xiao et al., 2018).

Transcriptional signatures are widely used to identify and classify cells, particularly those governed by marker genes or transcription factors driving cellular programs (Andrews and Hemberg, 2018; Shekhar and Menon, 2019). Levels of specific mRNAs drive protein expression, the formation or alteration of protein complexes, and ultimately the assembly and organization of subcellular structures that perform the functions specific to cell types and a variety of developmental and physiological cell states they can occupy. Several studies have addressed the relationship between RNA abundance and protein abundance, with Spearman (non-parametric) correlation values averaging from 0.4–0.7 (Edfors et al., 2016; Genshaft et al., 2016; Gut et al., 2018; Lundberg et al., 2010; Nusinow et al., 2020; Peterson et al., 2017; Popovic et al., 2018; Schulz et al., 2018). However, there is little precedent for relating RNA abundance to organization of cellular structures (Gut et al., 2018; Popovic et al., 2018) or function (Weber et al., 2020).



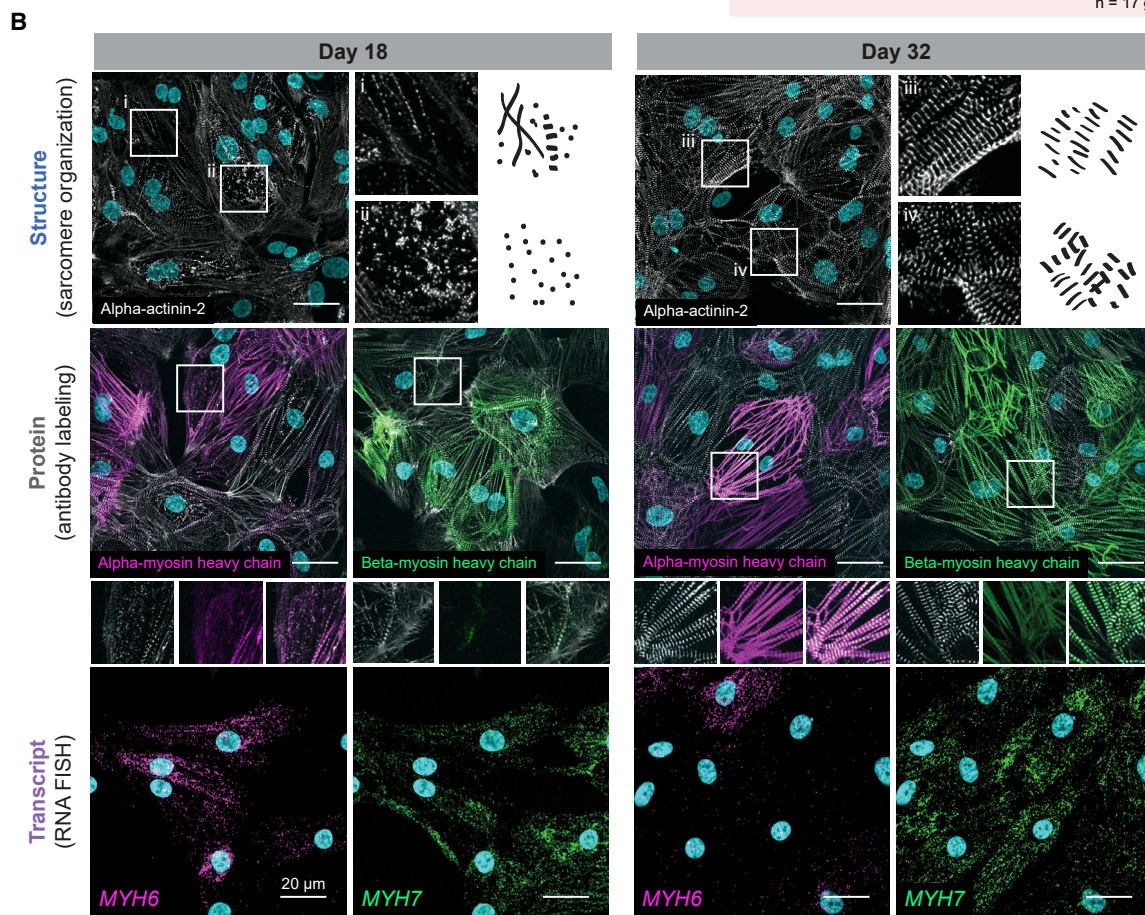
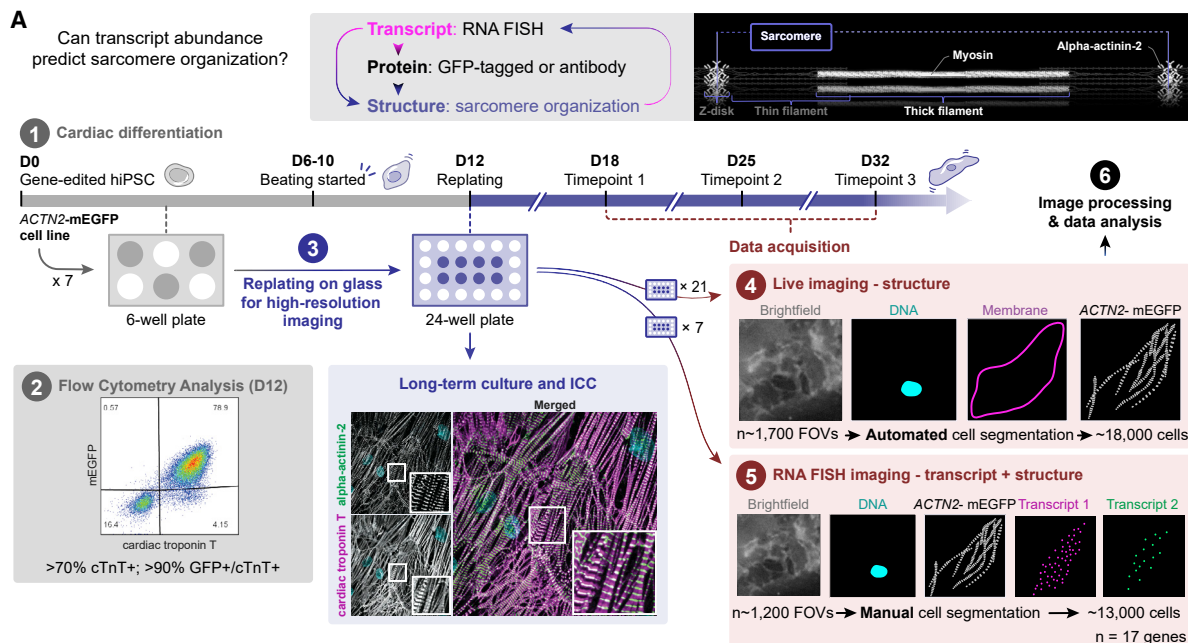


Figure 1. hiPSC-derived cardiomyocytes as a model system for studying the relationship between transcript abundance and cellular organization

(A) Top: schematic showing approach to predict sarcomere organization based on transcript abundance in hiPSC-derived cardiomyocytes. Right panel depicts the structure of a sarcomere, which is composed of thick and thin filaments, and alpha-actinin-2, located at the z-disk.

(legend continued on next page)

The goal of our study was to explore the relationship between RNA abundance and cellular organization by measuring both in the same cells. At one extreme, RNA abundance profiles and cell structural profiles may be tightly coupled such that the cell's structural organization (a proxy for cell phenotype) can be predicted from its gene expression, and vice versa (Liu et al., 2019; Popovic et al., 2018). However, gene expression and structural classifications may be connected more subtly, if at all. We hypothesized that cell organization and gene expression are complementary. Thus, combining both measurements might reveal clearer and more meaningful descriptions of cell states than either alone.

To explore these ideas, we used individual human induced pluripotent stem cell (hiPSC)-derived cardiomyocytes as a model cell type to test the extent to which RNA abundance of key genes correlates with the organizational state of the sarcomeres, the structure that powers contraction and is a hallmark of cardiac development *in vivo* and *in vitro* (Chopra et al., 2018; Fenix et al., 2018; Sanger et al., 2005) and built an automated image classifier that could be used to visualize and score both local and global myofibrillar organization within single cells. This dataset, comprising ~2,900 individual images and >30,000 individual cardiomyocytes, revealed the heterogeneity in structural states present within the cell population at single time points and the increasing degree of cellular organization that occurs over time as differentiation progresses. Our workflow systematically captured, quantified, and analyzed 4.35 TB of data, now publicly available as a Quilt package (see [data and code availability](#)), and enabled a cell-by-cell assessment of how the abundance of key transcripts relates to sarcomere organization.

Here, we show that measuring both transcript abundance and subcellular organization in single cells reveals cell states that cannot be identified with either measurement alone. Across carefully produced cell populations designed to maximize homogeneity, we observe a range of organizational stages, transcript levels, and correlations between the two. These data demonstrate that substantial variation in cell states exists within a single, rigorously quality-controlled, and standardized cell system as described in this study. The integrated framework described here incorporates multiple image-based analysis tools to robustly quantify structural organization in single cells in a way that goes beyond manual annotation or qualitative assessments and approaches the complexity that is common to scRNA-seq analysis. In total, this work illustrates the challenge of defining "cell state" objectively. We posit that any biologically

meaningful definition of cell state requires quantitative, multidimensional observations of single cells that account for space, time, and functionally diverse genes and proteins. Moreover, these observations should be taken at a sufficiently large scale to describe the distribution of behaviors present within the cell population.

RESULTS

A model system for single-cell analysis of structural organization and transcript abundance

Here, we describe a model system to integrate image-based measurements of structural organization and gene expression with the goal of detecting associations between them (Figure 1A, top panel). We chose hiPSC-derived cardiomyocytes because they undergo well-documented gene expression transitions as well as stereotypical structural changes during differentiation that can be captured by imaging. We focused our image-based analysis on the sarcomere, a cardiomyocyte structure that is essential for cardiac contractile function (Figure 1A, top right panel).

The sarcomere is composed of many proteins that form a highly regular structure that becomes increasingly organized over time during differentiation and maturation both *in vivo* and *in vitro* (Cui et al., 2019; Kamakura et al., 2013; Lundy et al., 2013; Pervolaraki et al., 2018; Snir et al., 2003; Van Meer et al., 2016; Veerman et al., 2015). Alpha-actinin-2 is commonly used as a marker to visualize the sarcomere (Luther, 2009; Pasqualini et al., 2015; Sheehy et al., 2014). We used an endogenously tagged and previously validated ACTN2-mEGFP hiPSC line for this study because it provides a robust readout for image-based structural analysis of the sarcomere (alpha-actinin-2-mEGFP-tagged cardiomyocytes, Figure 1A, top right panel (Roberts et al., 2019)). The development of this cell line included extensive characterization of both the undifferentiated stem cell cultures and their cardiomyocyte derivatives, ensuring that the resulting cells met the highest standard of quality control measures described previously (Roberts et al., 2017). We used an optimized small molecule protocol to induce differentiation of ACTN2-mEGFP hiPSCs into cardiomyocytes for imaging with high efficiency ($78.1\% \pm 3.7\%$ cardiac troponin T+ by flow cytometry, Figure 1A, part 1–2 and Figures S1B–S1E; Table S1) (Lian et al., 2012, 2013). By enabling tight control of cellular differentiation and cell maturation, this system made it possible to survey a large number of individual cells within the cell population over time.

(A1) Differentiation and re-plating timeline for cell populations used in the analyses; seven independent experiments were used in this study (Figure S1C; Table S1).

(A2) Flow cytometry for quality control of cardiomyocyte differentiation performed at D12 to determine the proportion of cardiomyocytes (cardiac troponin T [cTnT+] cells) in differentiated populations.

(A3–A5) (A3) Replated cells showing localization of cardiac troponin T by immunocytochemistry (ICC) and endogenously tagged alpha-actinin-2. Cells from several differentiation experiments were used for two separate workflows: (A4) schematic illustrating the imaging of live cardiomyocytes with labeling of the plasma membrane and nucleus, as well as automated cell segmentation and (A5) fixation and RNA fluorescence *in situ* hybridization (RNA FISH) of key genes prior to imaging for both transcript abundance and alpha-actinin-2-mEGFP protein. Cells in this dataset were manually segmented. FOV, field of view.

(B) Representative images of structure, protein, and transcript in cardiomyocytes. Top row shows alpha-actinin-2-mEGFP cells at D18 (left) and D32 (right); insets illustrate variation in alpha-actinin-2 patterns observed at these timepoints and a schematic illustration of these observed patterns. Insets are $20\ \mu\text{m} \times 20\ \mu\text{m}$. Middle rows show alpha-actinin-2-mEGFP cells stained for alpha- (magenta) and beta-myosin (green) protein in D18 and D32 cells. Insets illustrate variation in patterns and co-localization of the alpha-actinin-2-mEGFP protein and alpha- and beta-myosin. In all panels, localization of alpha-actinin-2-mEGFP is shown in white. Bottom row illustrates transcripts visualized by RNA FISH for MYH6 (magenta) and MYH7 (green) in D18 and D32 cells. Scale bar, $20\ \mu\text{m}$; insets are $20\ \mu\text{m} \times 20\ \mu\text{m}$.

We also developed a reproducible workflow that began with the re-plating of cardiomyocytes for imaging and included monitoring the cells for high survival, good morphology, beating, and the expression of the endogenous alpha-actinin-2-mEGFP protein (Figures 1A, part 1, 3 and S1A). Sarcomeric localization at the z-disk of alpha-actinin-2 was previously validated (Roberts et al., 2019). Antibody labeling of additional sarcomeric proteins (i.e., myosin light chain 2a, titin, alpha-myosin heavy chain, and beta-myosin heavy chain) further confirmed the integrity of the sarcomere in these tagged cells (Figures 1A, 1B, and S1A). Cardiac cells that passed the quality control process were then subjected to an experimental and computational workflow for capturing and analyzing all the image-based data across experiments. This workflow encompassed high-resolution imaging for structural analysis and multiplexed RNA FISH followed by image processing and data analysis (Figures 1A, part 4–6 and S1F, and S1G).

Analysis of distinct transitions of RNA, protein, and cellular structure

The hiPSC-derived cardiomyocytes mature during the differentiation process, resulting in structural changes to the sarcomere (Kamakura et al., 2013; Lundy et al., 2013). To relate gene expression to structural changes by imaging, we chose days 18, 25, and 32 (referred to as D18, D25, and D32) as time points that were amenable to high-resolution imaging based on previous work by us and others (Dunn et al., 2019; Roberts et al., 2019; Snir et al., 2003). We observed heterogeneity in the organization of the sarcomere at both the D18 and D32 time points as expected for immature hiPSC-derived cardiomyocytes (Kamakura et al., 2013; Lundy et al., 2013; Snir et al., 2003), with a progression to more organized and aligned sarcomeres over time (Figures 1B and S1A). Therefore, we focused most of the analysis in this study at the D18 and D32 time points, with D25 serving as an intermediate time point in some cases.

We performed antibody labeling for two key sarcomeric proteins in addition to alpha-actinin-2: alpha-myosin heavy chain (encoded by the gene *MYH6*) and beta-myosin heavy chain (encoded by the gene *MYH7*). Analysis of scRNA-seq data in a complementary dataset showed that the combination of *MYH6* and *MYH7* transcript expression alone is sufficient to correctly assign hiPSC-derived cardiomyocyte into a day 12 or day 24 time point with 84% accuracy, compared with 68% for a randomly selected 2-gene set and 97% for the top 40 time-dependent genes (Grancharova et al., 2021). This demonstrates that the expression levels of *MYH6* and *MYH7* represent the two highest ranked genes for interrogating correlations between gene expression and cellular organization in this system. Moreover, the switch in expression from the alpha to the beta isoform of the myosin heavy chain is associated with the maturation of human ventricular cardiomyocytes and has also been described in differentiating and maturing hiPSC-cardiomyocytes (Bouvagnet et al., 1987; Gorza et al., 1984; Liu et al., 2018; Redd et al., 2019; Ronaldson-Bouchard et al., 2018). We confirmed these observations in the alpha-actinin-2-mEGFP-expressing cardiomyocytes (Figure 1B, protein panel). We found sarcomeric localization of both proteins and co-localization with alpha-actinin-2-mEGFP.

We next evaluated the expression switch from *MYH6* to *MYH7* at the transcript level using RNA FISH for these two genes. This

analysis revealed heterogeneity in expression profiles for *MYH6* and *MYH7* across single cells within both time points and a trend toward decreasing *MYH6* expression relative to cells expressing *MYH7* from D18 to D32 (Figure 1B). This was consistent with a parallel but independent analysis of sc RNA-seq data (Grancharova et al., 2021) and previous studies (Chopra et al., 2018; Fenix et al., 2018; Weber et al., 2016, 2020). Taken together, this series of imaging experiments with the associated quality control measures validated our platform for image-based analysis of structure and gene expression. Furthermore, the changes in both gene expression and structural organization from D18 to D32 and the cell-to-cell heterogeneity observed for both readouts offered a unique opportunity to relate RNA abundance to sarcomeric organization in our system.

An automated classifier to distinguish stages of myofibrillar organization

To quantify stages of sarcomere organization in cardiomyocytes expressing mEGFP-tagged alpha-actinin-2 (Roberts et al., 2019), we leveraged the knowledge of expert annotators in combination with measurements of alpha-actinin-2 patterns to develop an automated, scalable method for assessing cell organization, which we termed the combined organizational score (COS). We used a three-step approach that included: (1) developing a machine-learning based tool to measure local organization; (2) applying an image autocorrelation method to quantify global alignment; and (3) combining the local and global organization metrics with cell morphological measurements to generate a linear model that predicts manual expert classifications. The model in the third step was developed to harness the information provided by the expert classifications while providing a finer quantitative discrimination between organization states than is possible by manual analysis. The population of cardiac cells used for this three-step analysis exhibits a range of sarcomere organization varying among individual cells at all time points, with increasing myofibril organization over time (Figures 1B and S1A).

As an initial step toward building a combined metric, we created a training dataset of 4,823 cells that were manually segmented and assigned an organization score by two experts. Each cell was scored from 1 (less organized, sparse, and punctate structures) to 5 (more organized, with the majority of cell area covered in regular z-disks, and well aligned along a single axis, Figures 2A, S2I, and S2J Dunn et al., 2019; Eschenhagen and Carrier, 2019; Qian et al., 2013). Expert scoring showed a clear trend of increasing organization between the D18 and D32 time points (Figure S2I). While there is precedent for a manual approach to quantifying sarcomeric organization (Dunn et al., 2019) and quantifying alignment and regularity of z-disk organization (Bray et al., 2008; Morris et al., 2020; Toepfer et al., 2019), we aimed to develop a high-throughput method to quantify the sarcomere organization stages observed in immature hiPSC-cardiomyocytes to a finer degree. Achieving this goal consistently for a large number of cells required an approach that captured both the local patterns of alpha-actinin-2 associated with the sarcomere including z-disks, puncta, fiber-like structures, and myofibrillar alignment (Figure 2B; Bray et al., 2008; Morris et al., 2020; Pasqualini et al., 2015; Toepfer et al., 2019). Therefore, we devised a quantitative and scalable method for measuring alpha-actinin-2 patterns that reports on local organization and served as the first module of the COS. We trained a

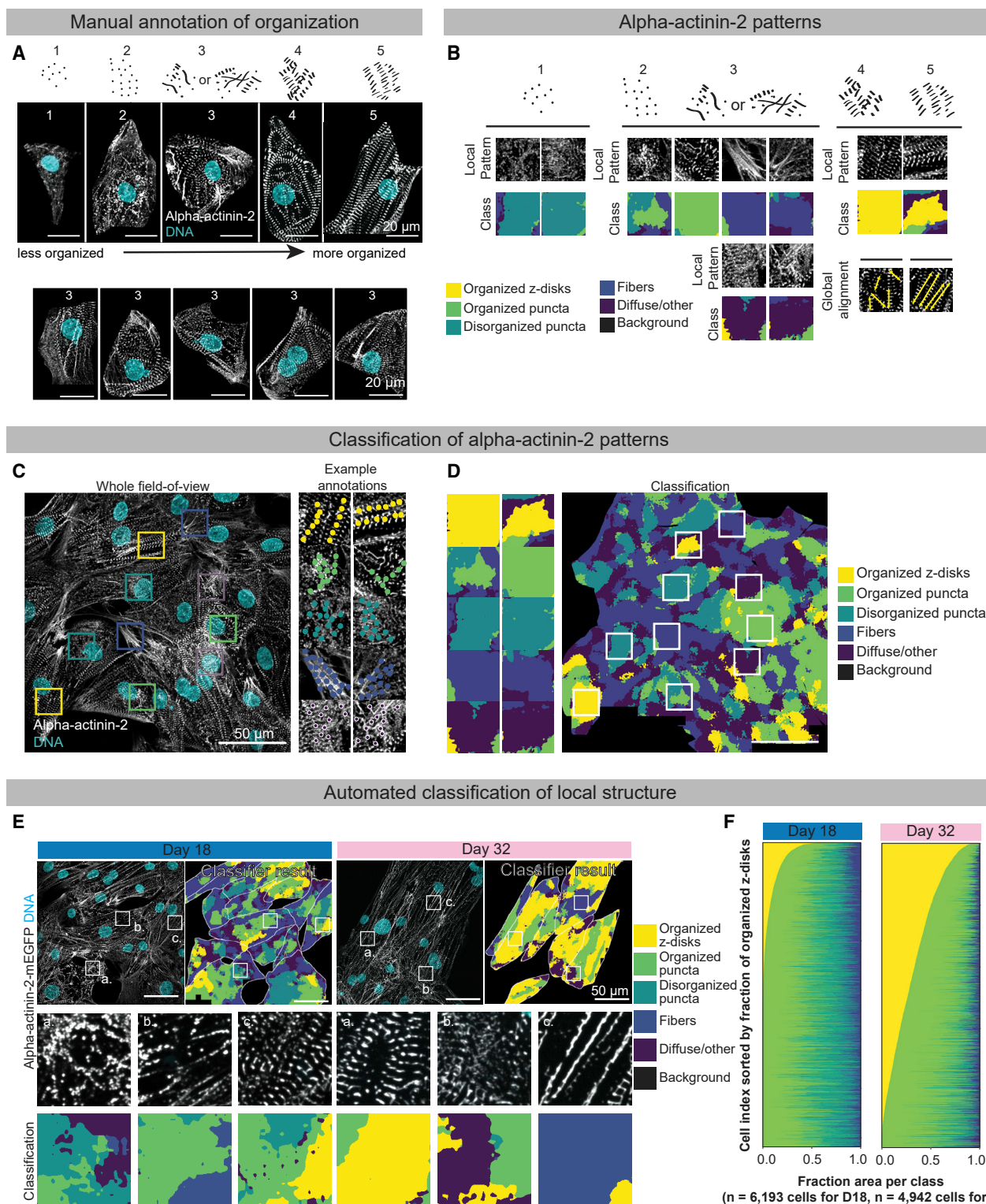


Figure 2. Classification and quantification of local patterns of alpha-actinin-2 organization using a deep-learning algorithm

(A) Manual scoring of myofibril organization based on alpha-actinin-2 patterns. Variation in alpha-actinin-2 organization in individual cells was manually scored by two experts and categorized into 5 organizational classes ranging from least organized (sparse, punctate structures), score of “1,” to most organized (majority of cell area covered in regular z-disks well aligned along a single axis), score of “5.” Many cells were annotated as “3”’s because of their exhibition of mixed patterns, as shown in the lower row of images. Example cells were cropped from full field-of-view images based on manual annotation of cell boundaries. Scale bar, 20 µm.

(legend continued on next page)

pixel-based deep-learning classifier to assign regions of each cell to one of six common patterns of alpha-actinin-2 organization, ranging from background (no visibly organized signal) to the highly regular z-disks observed for well-organized myofibrils (Figures 2B–2D). This automated model achieved 83% accuracy in categorizing the local organization of alpha-actinin-2 in subcellular regions into each of the six classes (Figures S2C–S2F). We then applied this classifier across the entire dataset consisting of 29,180 live and fixed cardiomyocytes (Figures 2E and 2F showing fixed dataset; Figure S2H showing live dataset). As expected, the analysis showed an increased number of cells with a regular z-disk pattern at the later time point (Figures 2F and S2H, yellow). We further validated this classifier by calculating the correlation for each organization class across experiments and images from live and fixed cells. All classes were strongly correlated between live and fixed with Pearson correlations ranging from 0.85–0.92 for each class (Figures S2A and S2B). This classifier of local organization confirmed and quantified the wide range of cell-to-cell variations in sarcomeric organization observed visually (Figure 2E) while providing a finer separation of structural features than was achieved by manual scoring. Additionally, this classifier generalized well across both fixed and live cell data across multiple time points (Figures S2G and S2H).

For the second module of this approach, we implemented a previously described global alignment measurement (Sutcliffe et al., 2018) that captured the large-scale alignment of myofibrils, an important attribute of overall structural organization of cardiomyocytes not captured by the local structural metric. The three global order parameters comprising this measurement describe the regularity, alignment, and spacing of the myofibrils within each individual cell independent of the total number or density of myofibrils (Figure 3). We observed a range of global alignment as shown in the representative example cells. These include cells exhibiting few regular z-disks and low global alignment (Figure 3Ai), many regular z-disks and low global alignment (Figure 3Aii), and many regular z-disks and high global alignment (Figure 3Aiii). The cross-correlation function (see STAR methods for details of calculation) displayed a fast exponential-type decay in cells with no regular patterns (Figure 3Bi), whereas a mix of exponential decay and oscillatory behavior was observed in cases where a preferential direction of alignment was present (Figure 3Biii). The correlation function oscillated when regular patterns with no preferential direction of alignment were present (Figure

3Bii). The Haralick correlations (Haralick, 1979) generate three key metrics for each cell based on global alignment: peak distance (Figure 3C), peak height (Figure 3C), and maximum coefficient of variation (Figure 3D). Peak distance was equivalent to sarcomere length, and the 1.5–2-μm alpha-actinin-2-mEGFP band spacing observed (Figure S3A, bottom right histogram) for most cells corresponds to the expected range of sarcomere length for hiPSC-derived cardiomyocytes (Lundy et al., 2013; Rodriguez et al., 2014). The median peak distance value showed an expected slight increase as the cardiomyocytes became more organized (Figure S3A, lower right histogram). We compared both live and fixed cell data as part of the validation of this metric and found a high degree of correlation between the same cells that had been imaged live and fixed (Figure S3B). Combining the global structural alignment metrics with the local features from the first module preserves two types of information important for describing cell heterogeneity using an integrated metric (Figures 3E and 3F).

For the third and final step, we calculated a COS by fitting a linear regression model that predicts the expert manual annotation scores using the local structural organization and global structural alignment metrics in addition to several direct measurements of cell features (i.e., the projected cell area and aspect ratio, Figure 4, step C). Our goal was to create a simple model that includes human interpretable features, as schematically illustrated in Figure 4. The expert annotation served as the ground truth for this linear regression model because we wanted the combined metric to capture the structural heterogeneity discernable to expert annotators (Figure 4, step B). The output of this model was a single weighted quantitative metric: the COS (Figure 4, step G). Each of the individual metrics was weighted differently in its contribution to the regression model to predict expert annotation, which reflected a feature's influence on the model's prediction of expert score (Figure 4, step F; Table S2). The z-disks were the most highly weighted metric in this linear model with a regression coefficient of 0.39. In contrast, the fibers showed the most negative regression coefficient of 0.32. This is consistent with imaging data showing that the proportion of fibers decreased over time as the organized puncta and z-disks gained prominence (Figure 2F). Cell area had a positive coefficient (0.19), suggesting that increasing cell size was associated with greater cell organization, as reported by others (Denning et al., 2016; Karbassi et al., 2020; Snir et al., 2003). We validated the expert trained model by scoring

(B) Expert annotators identified five distinct patterns of alpha-actinin-2 organization used to distinguish cell organizational classes. These correspond to organized z-disks (wide, regularly oriented bars, yellow), organized puncta (dots with a clear axis of organization, green), disorganized puncta (dots without a clear axis of orientation, teal), fibers (long, thread-like patterns, blue), and diffuse/other patterns (diffuse or overlapping areas with no clear organizational pattern, purple). Representative example annotations are shown for each class. In cells labeled “4” or “5,” experts looked for global alignment representing an additional, quantifiable dimension of organization (Figure 3).

(C) Example annotations of five distinct patterns of alpha-actinin-2 organization identified by a human annotator. Representative example annotations are shown as insets from the whole field-of-view image. Scale bar, 50 μm; image insets are 20 μm × 20 μm. Colors represent organizational class, as in (B).

(D) Results of the deep-learning-based classification of local structural organization in the whole field-of-view image and sub-regions shown in (C). Scale bar, 50 μm; image insets are 20 μm × 20 μm. Colors represent organizational class, as in (B).

(E) Deep-learning-based classification of local structural organization of alpha-actinin-2-mEGFP. Representative fluorescent images from two time points of cardiac differentiation displaying various alpha-actinin-2-mEGFP organizational patterns within a representative field-of-view image with cell segmentations. The original image is shown juxtaposed to the image illustrating the classifier results (top panel) for both time points. Header colors indicate cell age (D18: blue, D32: pink). Insets in the middle panel show examples of specific organizational features present in each population (labeled a, b, and c). The bottom row shows examples of the classifications for each inset: organized z-disks, organized puncta, disorganized puncta, fibers, and diffuse/other or background. Scale bar, 50 μm; image insets are 20 μm × 20 μm.

(F) Heatmaps from two time points in which individual cells (x axis) have been ranked according to the fraction of the cell area consisting of organized z-disks (yellow). Colors within the heatmap represent the same organizational classes shown in (E). n = 6,193 cells (D18), n = 4,942 cells (D32).

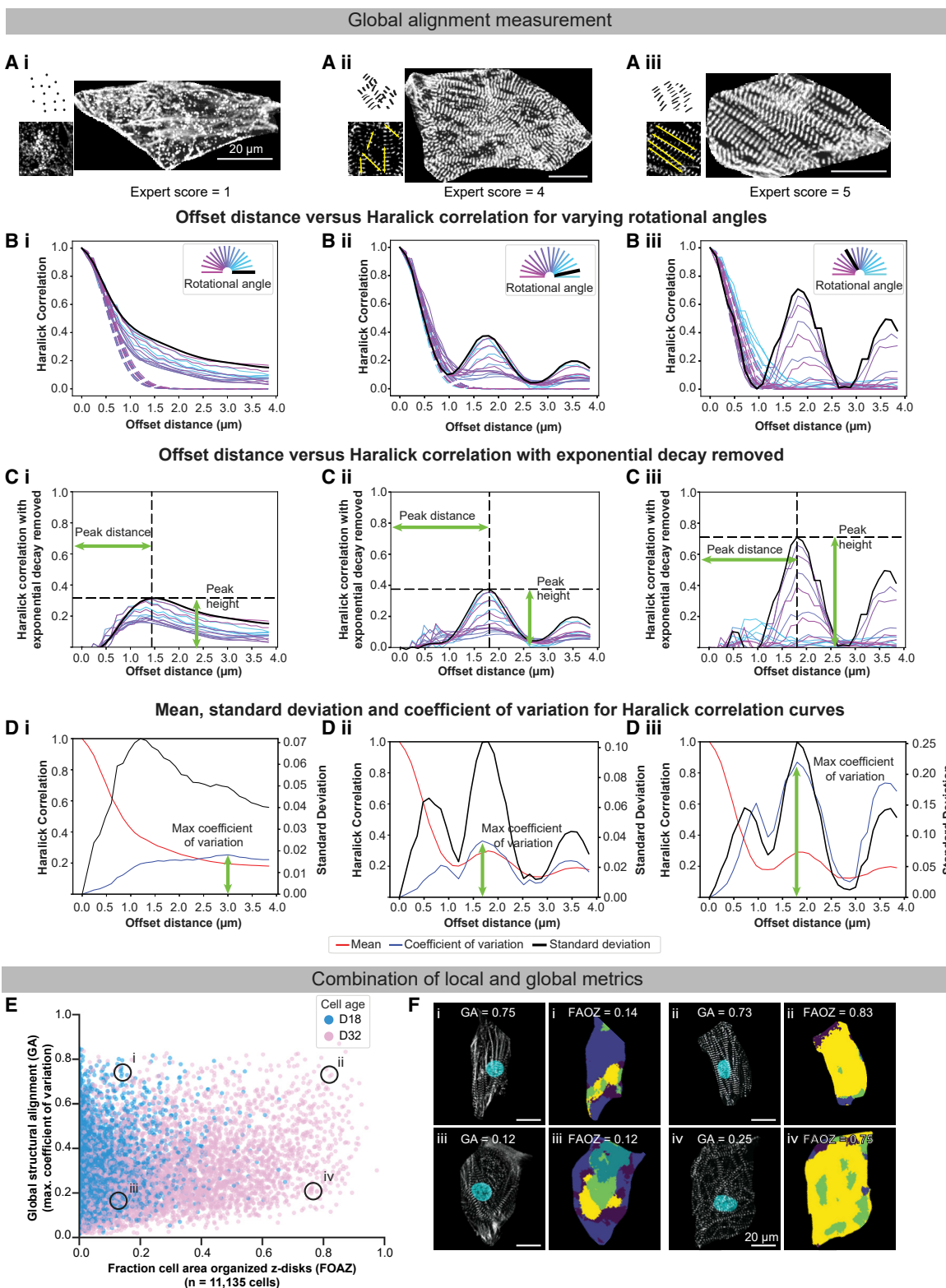


Figure 3. Quantification of global alignment of alpha-actinin-2 organization using Haralick correlation
 (A) Representative cells with low fraction of regular stripes and low alignment (Ai), high fraction of regular stripes and low alignment (Aii), and high fraction of regular stripes and high alignment (Aiii). Insets to the left of cells show schematized examples of the structure being quantified, and expert annotations are listed for each cell. Localization of alpha-actinin-2-mEGFP protein is shown in white. Scale bar, 20 μ m; image insets are 20 μ m \times 20 μ m.

(legend continued on next page)

approximately 1,000 new cells each from two separate test datasets (Figures 5A and S4A). A comparison of the regression model's performance (without re-weighting the model) on these two datasets showed that the expert-to-COS correlation was strikingly similar for both new datasets (correlations of 0.63 and 0.67, Figure 5A). This result verified that the COS could be reliably applied across multiple datasets and time points, allowing for the assessment of well-to-well and experiment-to-experiment variability (Figure S4E).

The resulting COS was consistent with the expert annotations. Furthermore, it produced a continuous quantitative metric that spread out the expert-assigned integer scores, an important objective for quantifying heterogeneity in organizational state (Figures 5B, S4C, and S4D). We further validated the COS by assessing its ability to separate cells with different organization states and found it spread out the single cells within these populations better than any individual metric alone, including the fraction of the cell containing organized z-disks or fibers, and resolved D32 from D18 cells more clearly (Figure 5B versus 5C and Figures S4B and 5D). These results confirmed the utility of the COS in our study using cells from different time points during differentiation and across experiments (Figures 5D and S4E). As expected, cells became more organized over time as reflected in the increasing COS (Figure 5D).

Quantifying the relationship between transcript abundance and structural organization in single cells

The path from RNA expression to sarcomere assembly encompasses many layers of post-transcriptional and post-translational regulation that are difficult to measure at scale in single cells. As a first step toward quantifying this relationship, we set out to co-measure both transcript abundance and cell organization in single cells and to determine whether RNA abundance correlates with sarcomere organization. Toward this goal, we used the image-based methodologies and workflows described in this study to capture, integrate, and analyze both structural (COS) and transcript abundance (RNA FISH) data from manually segmented single cells (Figure 6A; all data and code publicly available, see [STAR methods](#)). While we developed methods to automatically segment cardiomyocytes that utilize dyes

such as WGA (wheat germ agglutinin; [STAR methods](#)), we opted to manually segment cells when co-measuring myofibril organization with RNA FISH due to the limitation of fluorescence channels available for imaging.

We focused our analysis on a few genes across a large dataset of single cells in order to integrate gene expression with cell organization. To do this, we performed RNA FISH for 16 gene transcripts as multiplexed pairs in 11,135 alpha-actinin-2-mEGFP expressing cardiomyocytes at D18 and D32 (Figures S5A–S5C; Table S3). Five of these genes were chosen because of their association with known sarcomere biology at a structural, regulatory, or functional level and included *MYL7*, *ATP2A2*, *TCAP*, *NKX2.5*, and *BAG3* (Judge et al., 2017; Kasahara et al., 2003; Kubalak et al., 1994; MacLennan et al., 1985; Mason et al., 1999; Sacchetto et al., 2020). The remaining 11 genes were chosen based on results in a complementary transcriptomic study (Granchiarova et al., 2021), where groups of genes were identified for their ability to correctly assign cardiomyocytes to a selected time point, which included *MYH7*, *MYH6*, *COL2A1*, *H19*, *VCAN*, *CNTN5*, *MEF2C*, *PLN*, *PRSS35*, *BMPER*, and housekeeping gene *HPRT1* (Bargehr et al., 2019; Bertero et al., 2019; Friedman et al., 2018; Palpant et al., 2017) (Figures 6B–6E and S5A–S5C). Some of the genes in this second subset are also of known importance in cardiac biology (i.e., *MYH7*, *MYH6*, *PLN*, and *MEF2C*) and, thus, overlap in these two categories (Table S3). The number of genes chosen reflected our goal to focus our analysis on key genes alongside cell organization across a large dataset of single cells, a strategy supported by recent work suggesting that gene expression is effectively low dimensional, and that small groups of transcriptional programs can define a cell state (Heimberg et al., 2016).

Most of the genes tested showed a broad distribution of transcript abundance across the cell population for both the D18 and D32 cardiac populations. We found transcript count to be correlated with cell area across most assayed genes; thus, we report transcript abundance as density (counts/ μm^2 , Figure S6A, see [STAR methods](#)). We also observed cell-to-cell heterogeneity in structural organization (Figures 6B–6E, S5B, and S5C). To relate these two measurements, we calculated the Spearman rank correlation coefficient (r_s) between transcript abundance (RNA FISH

(B) (Bi–Biii) Offset distance versus Haralick correlation for varying rotational angles (solid lines, color corresponds to angle in diagram) and exponential fitting of curves (dashed lines) for cell categories described in (A). Bold black line in the inset and on plot highlights the curve for rotational angle with maximum correlation.
(C) (Ci–Cii) Offset distance versus the correlation of exponential fitting for cell categories described in (A), with the peak distance and peak height metrics indicated by green arrows.

(C) Peak value 0.32 at a distance of 1.44 μm for angle 0°.

(Cii) Peak value 0.37 at a distance of 1.8 μm for angle 12°.

(Ciii) Peak value 0.71 at a distance of 1.8 μm for angle 120°.

(D) (Di–Diii) Offset distance versus the mean, coefficient of variation, and standard deviation of the Haralick correlation for cell categories described in (A); the maximum coefficient of variation is indicated with a green arrow.

(Di) Maximum coefficient of variation equals 0.25.

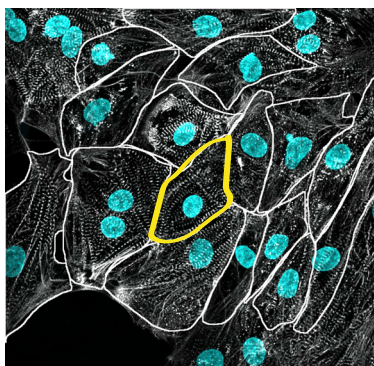
(Dii) Maximum coefficient of variation equals 0.36.

(Diii) Maximum coefficient of variation equals 0.87. See [STAR methods](#) for a complete description of calculations.

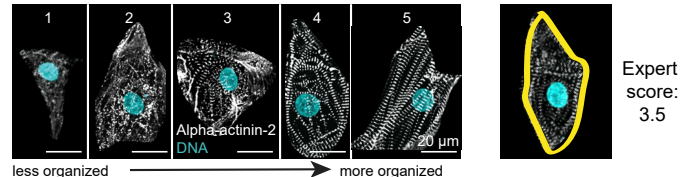
(E) Plot showing fraction of cell area covered with organized z-disks versus maximum coefficient of variation from Haralick correlation method (see “quantification of global sarcomere alignment” in [STAR methods](#) for details) at D18 (blue) and D32 (pink). Cells can be separated as being regularly aligned but containing few regular stripes or as having high proportions of regular structure and being well aligned. Examples of these organizational patterns are shown in (F) and indicated by circles. n = 11,135 cells.

(F) Example cells are shown from each quadrant of the graph in (E), showing localization of alpha-actinin-2-mEGFP protein (white) and nuclei (cyan). Global alignment (GA) value and fraction of area covered in organized z-disks (FOAZ) is indicated for each example cell, with color coded organizational regions representing the same organizational classes shown in Figure 2E. Example cells were cropped from full field-of-view images based on manual annotation of cell boundaries. Scale bar, 20 μm .

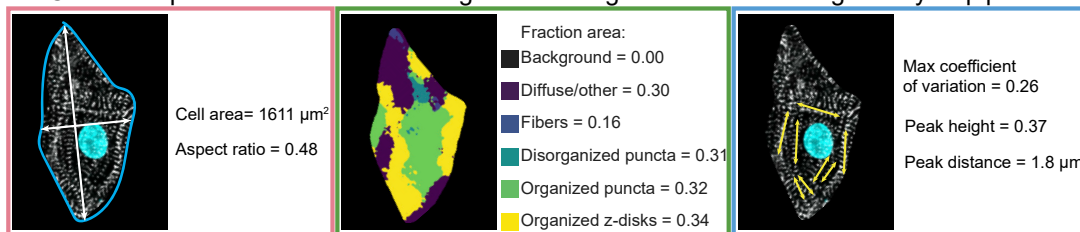
A Manually annotate cell boundaries in whole FOVs



B Use discrete expert scores as ground truth



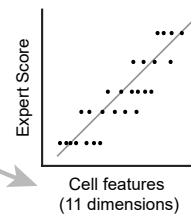
C Calculate quantitative features of single cells using an automated image analysis pipeline



D Weight expert score by number of cells in discrete score bins

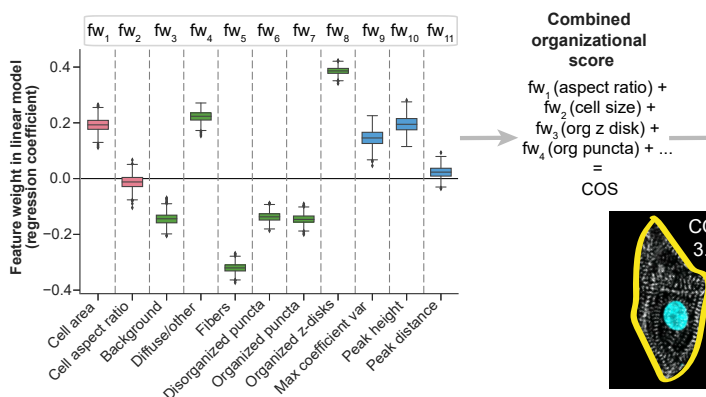
Expert score	n cells
1	413
2	982
3	4326
4	876
5	102

E Fit linear model of weighted expert scores as a function of 11 calculated cell features



F Obtain feature weight (fw) from regression

■ Cell features ■ Local organization ■ Global alignment



G Use linear model to calculate COS for all cells

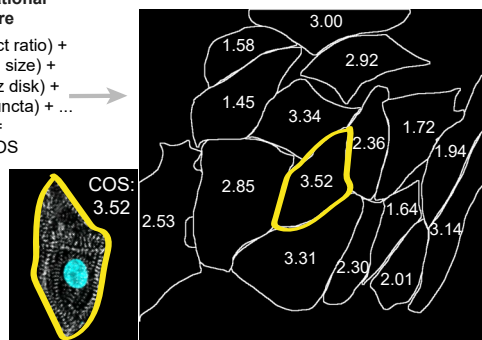


Figure 4. Workflow for establishing the combined organizational score

(A) Cell boundaries are manually annotated in whole field-of-view images using Napari.

(B) Two experts score individual cells based on alpha-actinin-2 expression and organization with an integer value ranging from "1" (less organized) to "5" (more organized). Each cell receives two independent scores that are averaged to establish the ground truth. Example cell (yellow outline throughout) was scored as a "3" by one expert and as a "4" by another expert, yielding an expert score of 3.5. See Figure 2A and corresponding text for more details.

(legend continued on next page)

density, counts per μm^2) and structural organization (COS) for each of the 11,135 cells. To decouple changes in transcript abundance that were only associated with cell age from changes associated with cell organization state, we calculated the r_s for the D18 and D32 cell populations separately as well as for the combined cell population (Figures 6B and S5A; Table S4).

We identified several types of relationships between gene expression and cell organization from this analysis. One of these relationship classes included genes that change in transcript abundance over time (exhibiting a positive or negative correlation between timepoints and, therefore, a higher correlation for the “all” category) but do not show a correlation with structural organization at either time point individually. *COL2A1* represents one of these genes, with a decrease in transcript abundance from D18 to D32 and no correlation with COS at either time point despite the presence of organized cells in both populations ($r_s = -0.07$ at D18, $r_s = -0.05$ at D32, Figures 6B and 6C). When considering both time points combined, there is a strong negative correlation between gene expression and structure that is most likely driven by the concurrent increase in structural organization with the pronounced decrease in transcript abundance ($r_s = -0.40$, Figure 6B, gray boxplot). Another example of this trend, but with a positive correlation, is *PLN*, the gene that encodes phospholamban, a membrane protein that regulates the cardiac sarcoplasmic reticulum calcium-ATPase (SERCA). *PLN* showed a weak positive correlation with structural organization at either time point ($r_s = 0.09$ at D18, $r_s = 0.16$ at D32) and a strong positive correlation for the combined cell population ($r_s = 0.46$, Figure 6B, gray boxplot). This finding is consistent with the increase in transcript abundance of *PLN* with time (Figure 6E). Example cells from the two time points showcase this trend of increasing organization and transcript abundance with time (Figure 6E). *H19* had a similar trend to *PLN* (Figure S5A). This highlights the utility of our multi-modal approach to defining cell states and exposes the limitations to using gene expression as a stand-alone measurement. The transcript abundance of genes such as *COL2A1*, *PLN*, and *H19* can be used as a readout of time point but cannot be used to discriminate between organizational states of cells within a time point.

Another relationship we observed included genes that showed a correlation between structure and transcript abundance at both time points individually and together. This gene set includes

MYH7, which showed the strongest positive correlation for D32 ($r_s = 0.28$ at D18, $r_s = 0.44$ at D32), but did not exhibit a shift in gene expression over this time frame (Figures 6B and 6D). An example image from the two ends of this spectrum shows a representative D18 cell with low levels of *MYH7* transcript and poorly organized sarcomeres and a cell from D32 with high levels of *MYH7* transcript and well-organized sarcomeres. *TCAP* is another example of this category with a positive correlation at both time points as well as in the combined cell population (Figures S5A and S5B).

For some genes, we observed the strongest correlation in the combined cell population (gray boxplot) with a negative correlation in at least one time point. This trend suggests an age-related association of transcript abundance with structural organization. *MEF2C* and *MYH6* are two example genes from this category (Figures S5A and S5B). *MYH6* showed a strong negative correlation with organization in the combined (all) and the D18 population and a smaller negative correlation with organization at D32 ($r_s = -0.26$ at D18, $r_s = -0.14$ at D32; Figure S5A). The overall level of *MYH6* transcript expression decreased substantially from D18 to D32 as expected, and the net negative correlation for the two time points combined was modestly stronger than for either one alone (Figures S5A–S5C). Figures S5A and S5B show similar analysis for the remaining genes. Of these, *MLY7* is distinct with a positive correlation with cell organization at D32 ($r_s = -0.04$ at D18, $r_s = 0.27$ at D32, $r_s = 0.1$ in combined) despite a high transcript abundance at both time points. Some of the remaining genes showed no correlation between transcript level and organization irrespective of time point (e.g., *ATP2A2* and *PRSS35*) or did not fit clearly into any of the categories described above (e.g., *BAG3* and *NKX2-5*; Figures S5A and S5B).

The correlations described above provided a population level understanding of gene expression and structural cell states for the various time points individually and together. However, the image-based single-cell measurements of both transcript and organization also provided the opportunity to explore the nuanced relationship between the two measurements, cell by cell, within each population. For example, in cells that were probed for both *MYH6* and *MYH7*, transcript abundance for *MYH7* was positively correlated with structural organization as a population, but we also observed a few individual cells with high *MYH7* transcript and low levels of organization ($r_s = 0.33$

(C) Features are computationally extracted for all single cells. These include cell features (pink box; cell area, aspect ratio), local organization (green box), and global alignment (blue box). Local structural organizational features were derived from the automated alpha-actinin-2 classifier model and are composed of the fraction of the cell categorized as background (black), diffuse/other (purple), fibers (blue), disorganized puncta (teal), organized puncta (green), and organized z-disks (yellow). Global structural alignment features (blue box) capture information about the overall alignment of the alpha-actinin-2 structures within an individual cell; here we use the maximum coefficient of variation, peak height, and peak distance. See Figures 2 and 3 and corresponding text for more details regarding how these features are calculated. Feature values are listed for the example cell shown throughout (yellow outline).

(D) Each expert score of “1” through “5” for cell organization is weighted based on the number of cells in discrete score bins. This distributes scores before fitting the linear model. The number of cells (n) is given for each of the categories in the training set.

(E) A linear regression model fits the expert scores as a function of the 11 features shown in part 3. See Figure 5C for more details around model validation and performance on hold-out training and test datasets. See Figure S7 for models with transcript features (2 and 13 feature models).

(F) Relative contribution of features to the linear regression model used to calculate a cell’s COS. The weight (regression coefficient) is plotted for each feature and colored by feature type as described in part 3. Features and organizational score were calculated per segmented cell and used for further analysis. The training set contained both D18 and D32 cells ($n = 4,823$ cells in total, $n = 11$ total features). Box and whisker plot weights are based on 1,000 bootstrap resamples (see STAR methods). Units for features: cell area in μm^2 ; all local organization metrics (in green) as fraction of cell area; peak distance in μm .

(G) The linear model with regression coefficients for the 11 features was applied to the full dataset to calculate the COS, which is a continuous value, for all single cells. COS of example cell (yellow outline) was calculated to be 3.52. COS values for each of the cells in the FOV shown in part 1 are printed inside the corresponding cell boundary.

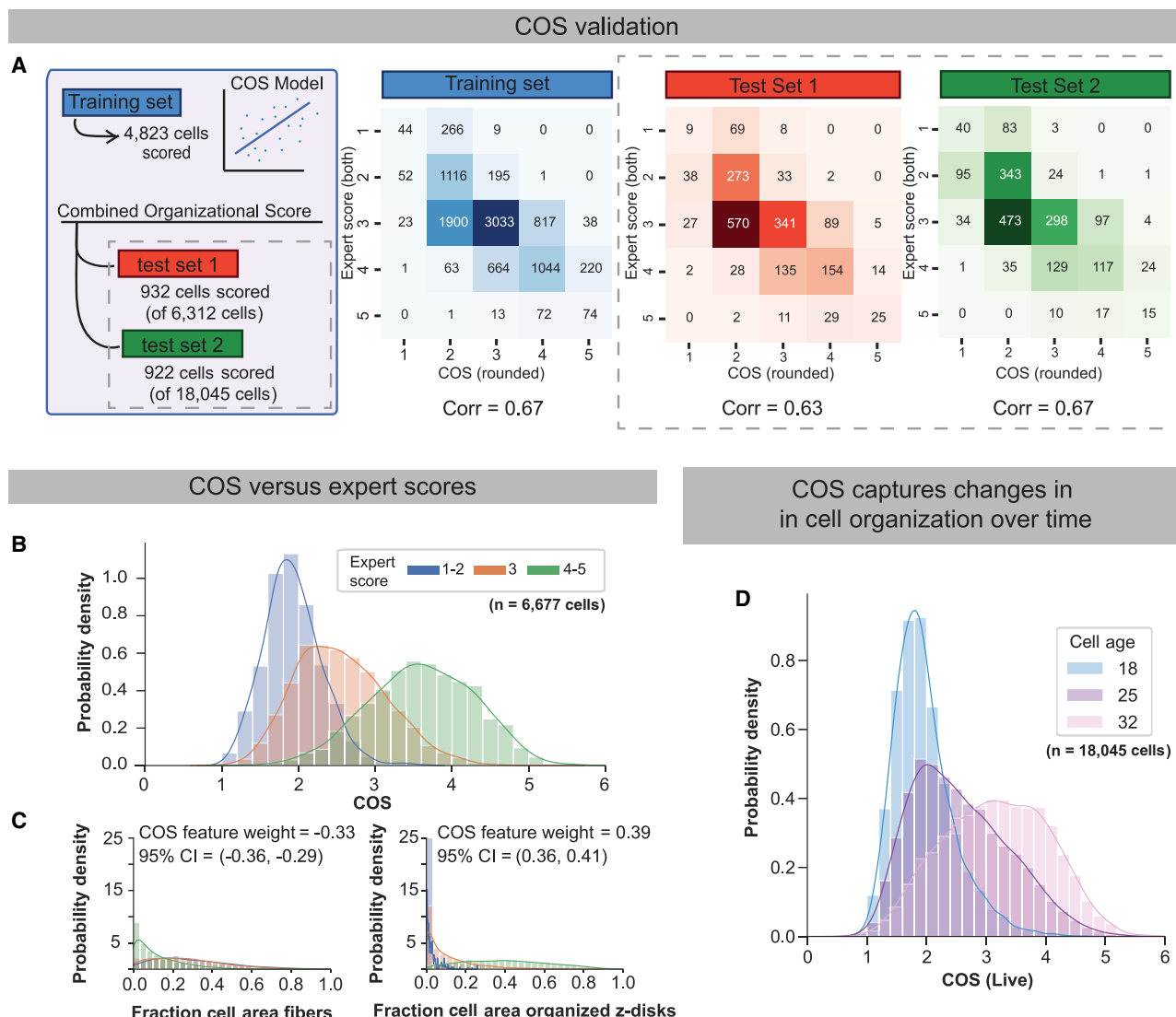


Figure 5. Quantifying cardiomyocyte organization at scale across datasets and timepoints using a single metric combining multiple cell features

(A) Left-hand schematic shows how the COS was trained on a single dataset and validated across multiple datasets. An initial training set of 4,823 cells was annotated by expert scorers; these scores were used to fit the linear regression model (weights shown in Figure 4, step F). Human experts then scored approximately 1,000 cells each from new separate datasets; the model was applied without re-weighting the regression coefficients to these new datasets. Confusion matrices show concordance between the COS (rounded to nearest discrete value) and include data from both expert annotators for the training set (blue) and test sets (orange and green). Overall Spearman correlation values between the COS and human scores are given below each confusion matrix.

(B) Histogram comparing the expert annotations of organization to the COS, colored by expert annotation score: 1–2 (blue), 3 (orange), or 4–5 (green). n = 6,677 cells, which includes cells from the training set (n = 4,823 cells), test set 1 (n = 932 cells), and test set 2 (n = 922 cells).

(C) Histogram comparing the expert annotations of organization to the fraction area organized z-disks and fraction area fibers, colored by expert annotation score: 1–2 (blue), 3 (orange), or 4–5 (green). n = 6,677 cells.

(D) Histogram showing the distribution of COSs for D18 (blue), D25 (purple), and D32 (pink) cells; COS score calculation was applied to cardiomyocytes that were imaged live across these three timepoints (shown in Figure 1, part 4). n = 18,045 cells.

at D18, $r_s = 0.25$ at D32, $r_s = 0.39$ combined population, MYH7–MYH6 relative abundance, Figures S5D and S5E; Table S4). Similarly, high abundance of MYH6 transcript was found in some highly organized cells despite the negative correlation to structural organization overall (Figures S5D and S5E).

Among the genes evaluated in this study, we found that the degree of myofibrillar organization was most correlated with

mRNA abundance of MYH7. This result is consistent with the switch from MYH6 to MYH7 expression expected during the time frame of increasing myofibrillar organization in our studies and others (Pioneer et al., 2016; Racca et al., 2016; Reiser et al., 2001; Xu et al., 2009; Yang et al., 2014). The correlation between mRNA abundance of MYH7 and the COS was 0.44 on day 32. We argue that this is notably correlated, given that direct

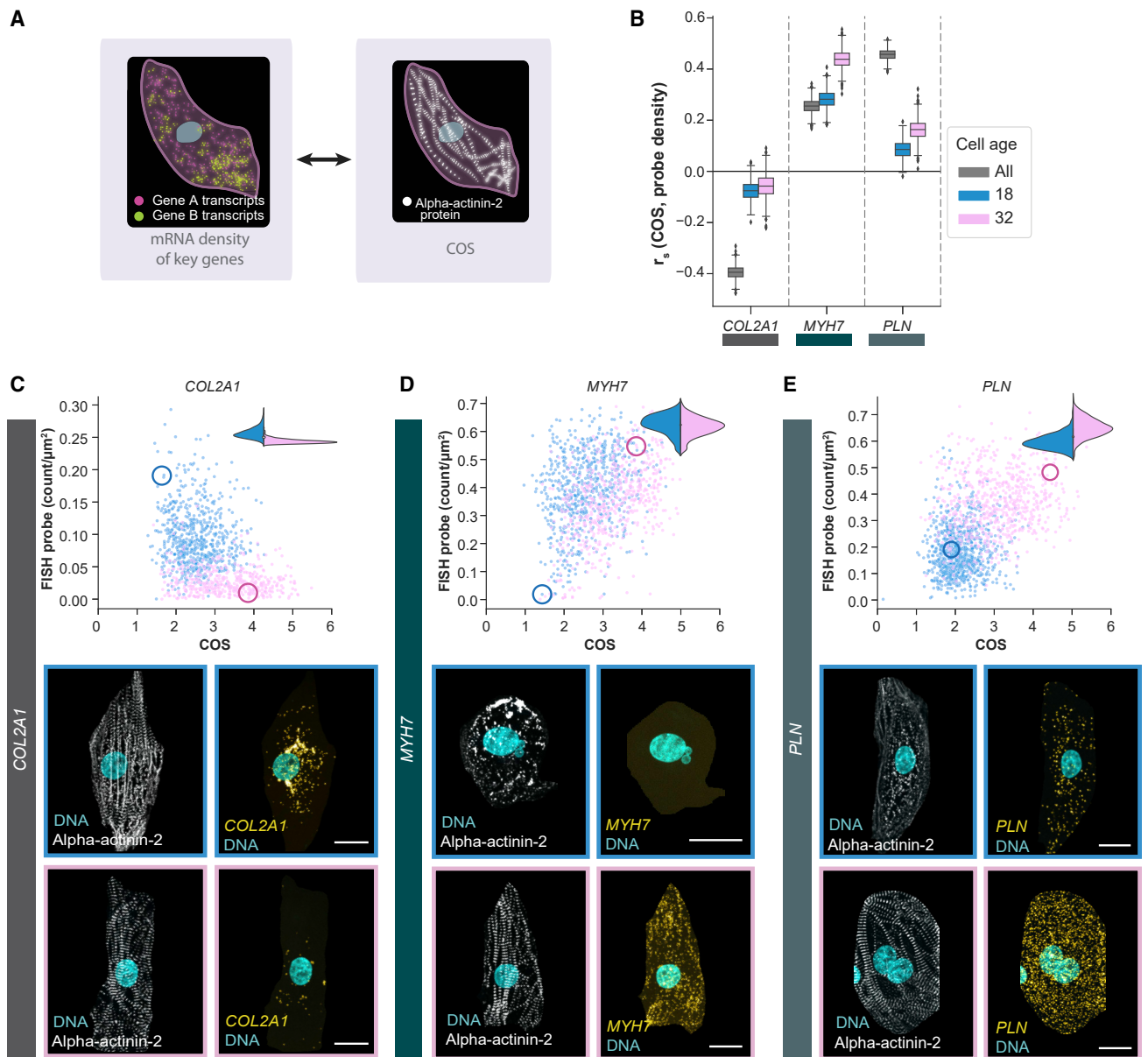


Figure 6. Measurement of correlation between combined organizational score and transcript abundance enables identification of genes that correlate with cell organization, timepoint, or both

(A) Schematic illustrating the experimental goal of establishing correlations between gene expression (measured by RNA FISH) and structural organization (measured by COS).

(B) Box plots showing the bootstrapped Spearman rank correlation between COS and transcript abundance of *COL2A1*, *MYH7*, and *PLN*. Correlation metrics are shown for each gene assayed by RNA FISH in alpha-actinin-2-mEGFP cardiomyocytes, for each time point as well as combined populations. Gray box plots indicate the correlation across all cells; blue and pink boxplots show the correlation for cells stratified by age (D18: blue, D32: pink). Mean Spearman rank correlations and 95% confidence intervals are listed in Table S4. Measurements where the bootstrapped interval crosses zero are not statistically significant.

(C) Scatterplot showing *COL2A1* transcript abundance from RNA FISH, reported as density (count/ μm^2) (y axis) versus COS (x axis). Transcript abundance is measured by FISH probe spot density (counts per μm^2) in single cells; each dot represents a single cell ($n = 717$ for D18, $n = 487$ for D32, $n = 1,204$ total cells). Density plot shows marginal distribution transcript abundance for D18 (blue) and D32 (pink) timepoints. Representative images shown for D18 cell (top row, blue box; coordinate circled on graph) and D32 cell (bottom row, pink box; coordinate circled on graph). Alpha-actinin-2-mEGFP protein localization (white) is shown on the left for each cell, *COL2A1* transcript ("yellow hot" LUT) is shown on the right, and DNA is shown in cyan. Scale bar, 20 μm .

(D) Scatterplot showing *MYH7* transcript abundance from RNA FISH, reported as density (count/ μm^2) (y axis) versus COS (x axis). Transcript abundance is measured by FISH probe spot density (counts per μm^2) in single cells; each dot represents a single cell ($n = 719$ for D18, $n = 578$ for D32, $n = 1,297$ total cells). Density plot shows marginal distribution transcript abundance for D18 (blue) and D32 (pink) timepoints. Representative images shown for D18 cell (top row, blue box; coordinate circled on graph) and D32 cell (bottom row, pink box; coordinate circled on graph). Alpha-actinin-2-mEGFP protein localization (white) is shown on the left for each cell, *MYH7* transcript ("yellow hot" LUT) is shown on the right, and DNA is shown in cyan. Scale bar, 20 μm .

(legend continued on next page)

measurements of RNA and protein across the genome have produced correlations in the range of 0.4–0.7 (Edfors et al., 2016; Genshaft et al., 2016; Gut et al., 2018; Lundberg et al., 2010; Nusinow et al., 2020; Peterson et al., 2017; Popovic et al., 2018; Schulz et al., 2018), and the assembly and organization of the contractile sarcomere is a highly dynamic and coordinated process that involves dozens of distinct proteins and protein complexes. However, the dominant conclusion to be drawn from these data is that the state of cellular organization is not based on gene expression alone, even for a gene such as *MYH7* for which expression is both correlated with and functionally associated with structural maturation of cardiomyocytes. To further investigate the relationship between *MYH7* transcript density and cellular organization, we modified the COS model to include two additional features: *MYH6* and *MYH7* transcript density, as predictors of expert score in addition to the 11 cell features in the original model (Figure 4C). An 11 feature model refit using only cells with RNA FISH for *MYH6* and *MYH7* ($n = 1,297$) performed similarly well to the previously described 11 feature model fit on all expert-scored cells ($n = 4,823$) (Figures S7A–S7C; Figure 4F; Figures 6B and 6D, S5A, and S5B). Including the transcript density of *MYH6* and *MYH7* (13 feature model) resulted in a very modest improvement in performance (Figures S7D and S7F) and similar Spearman correlations between expert scores and COS for the 13 and 11 feature models ($r_s = 0.665$ for 13 features; $r_s = 0.659$ for 11 features) (Figure S7G). Both of these models (11-feature model with only the *MYH6*/*MYH7* subset of cells, and 13-feature model including transcript abundance of *MYH6*/*MYH7*) performed better than a 2-feature transcript-only model (Figures S7E–S7G).

These results demonstrate that the COS provided a robust and systematic metric for defining relationships between RNA abundance and organization in single cells within a diverse population (Figure 7). The resulting analysis identified a variety of modes by which organizational features and gene expression states can co-vary. Additional measurements in single cells, such as protein levels, may further inform our understanding of cell states (Figure S6).

DISCUSSION

Many recent studies have performed scRNA-seq-based measurements of diverse cell populations, reduced the dimensions of these data, and assigned individual cells to biologically meaningful groups. However, it is unclear whether these groups represent cell types, cell states, or a mixture between the two. Moreover, although some cell types may be defined anatomically or by physiological function, quantitatively robust definitions of cell type and cell state are generally elusive.

Our study focuses on cardiomyocytes, a cell type that can be differentiated from hiPSCs and undergoes a process of differenti-

ation and maturation over extended time in culture or as engineered tissue, under carefully controlled conditions (Lundy et al., 2013; Ronaldson-Bouchard et al., 2018; Sacchetto et al., 2020). We provide a rigorously quality-controlled and standardized approach to quantify transcript abundance, local and global subcellular organization, and relationships between quantitative observations in tens of thousands of single cells (Figures 1A and 4). Our data demonstrate that substantial variation in cell states exists even within an experimentally controlled cell population designed to optimize homogeneity (Figure 7). We suggest that defining biologically meaningful cell states requires multidimensional and quantitative observations in single cells that consider spatiotemporal changes and functionally diverse genes and proteins, and that these measurements need to be performed at a large enough scale to capture the variation present in the population.

While the image-based tools we developed are specific for myofibril organization, analogous methodologies can be developed for other structures and cell types. For example, during cardiomyocyte maturation, ion channel isoform shifts may best be measured with transcriptomics or electrophysiology, whereas the enormous structural rearrangements in the intermediate stages of differentiation may be more readily classified by image-based analysis. Additional measurements, such as functional phenotype (force generation, electrophysiology, and metabolism for cardiomyocytes) might further sharpen the cell categorization (Weber et al., 2020). By combining these measures with larger subsets of genes using highly multiplexed FISH or *in situ* sequencing (e.g., MERFISH Chen et al., 2015; Wang et al., 2018; seqFISH Eng et al., 2019; CODEX Goltsev et al., 2018; or FISSEQ Lee et al., 2015), even more granular and meaningful classifications may emerge. Finally, an ultimate goal may be to expand this approach to include cell dynamics. Tracking live cells would show whether individual cells traverse the available state space over time or maintain a static state within the population. This study is a first step toward answering these questions and building an unbiased, quantitative, and image-based understanding of how transcriptional profiles relate to other phenotypes across populations of single cells.

STAR★METHODS

Detailed methods are provided in the online version of this paper and include the following:

- **KEY RESOURCES TABLE**
- **RESOURCE AVAILABILITY**
 - Lead contact
 - Materials availability
 - Data and code availability
- **EXPERIMENTAL MODEL AND SUBJECT DETAILS**
 - Cell lines and plasmids

box; coordinate circled on graph) and D32 cell (bottom row, pink box; coordinate circled on graph). Alpha-actinin-2-mEGFP protein localization (white) is shown on the left for each cell, *MYH7* transcript (“yellow hot” LUT [Look-Up Table]) is shown on the right, and DNA is shown in cyan. Scale bar, 20 μm . (E) Scatterplot showing *PLN* transcript abundance from RNA FISH, reported as density (count/ μm^2) (y axis) versus COS (x axis). Transcript abundance is measured by FISH probe spot density (counts per μm^2) in single cells; each dot represents a single cell ($n = 902$ for D18, $n = 672$ for D32, $n = 1,574$ total cells). Density plot shows marginal distribution transcript abundance for D18 (blue) and D32 (pink) timepoints. Representative images shown for D18 cell (top row, blue box; coordinate circled on graph) and D32 cell (bottom row, pink box; coordinate circled on graph). Alpha-actinin-2-mEGFP protein localization (white) is shown on the left for each cell, *PLN* transcript (“yellow hot” LUT) is shown on the right, and DNA is shown in cyan. Scale bar, 20 μm .

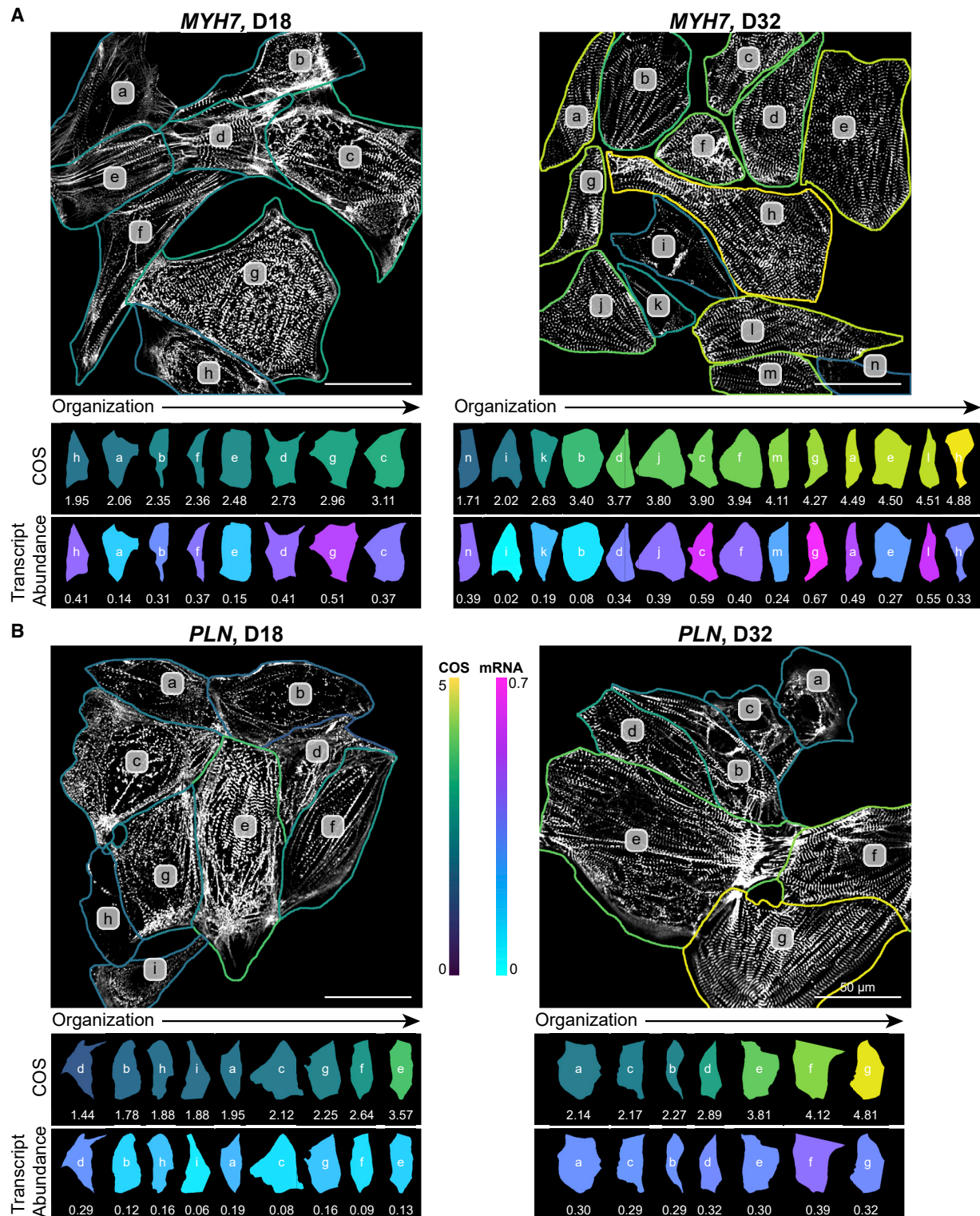


Figure 7. Diversity of cell states present within a population

(A) Representative field-of-view images of cells probed for *MYH7* showing alpha-actinin-2-mEGFP protein (white) with single cell outlines from manual annotation colored by each cell's COS. Single cells are shown and labeled below field-of-view images, colored by COS and transcript abundance. Cells are ordered by COS, with color bars in the center showing correspondence between color and COS or transcript abundance (shown below in B). COS and transcript abundance levels are listed below each single cell. D18, left; D32, right. Scale bar, 50 μ m.

(B) Same as above, but transcript abundance is shown for *PLN*. Color bars apply to (A) and (B). D18, left; D32, right. Scale bar, 50 μ m.

● METHOD DETAILS

- Human induced pluripotent stem cell culture
- Directed cardiomyocyte differentiation
- Single cell dissociation for replating onto glass
- Flow cytometry of samples for replating
- Replating cardiomyocytes for imaging and RNA FISH
- Cardiomyocyte immunolabeling for imaging
- WGA staining of live cardiomyocytes for imaging
- RNA FISH using HCR v3.0
- Cardiomyocyte imaging
- ML-based single-cell segmentation of WGA-stained live cardiomyocytes
- Manual cell annotations of FISH data in Napari
- DNA (Nuclear) segmentation in FISH samples
- RNA spot segmentation and feature extraction in FISH samples
- Expert annotation of cell organization
- ML-based alpha-actinin-2 pattern classification
- Quantification of global sarcomere alignment

● ALPHA-ACTININ-2 INTENSITY MEASUREMENTS

● FISH AND ALPHA-ACTININ-2 ASSAY DATA PREPARATION

- Linear model predicting expert organization scores from single cell metrics
- Bootstrapped confidence intervals
- Probability densities
- Correlation analysis
- Differential expression between *MYH6* and *MYH7*

● QUANTIFICATION AND STATISTICAL ANALYSIS

SUPPLEMENTAL INFORMATION

Supplemental information can be found online at <https://doi.org/10.1016/j.cels.2021.05.001>.

ACKNOWLEDGMENTS

We thank Joy Arakaki for flow cytometry analysis, Joyce Tang and Brian Long for RNA FISH method development, Colette DeLizzo and Haseeb Malik for cardiomyocyte maintenance and sample collection, Derek Thirstrup for CellProfiler guidance, and Thao Do for illustrations. We thank the Allen Institute for Cell Science team for helpful discussions and support. The WTC-11 line that we used to create our gene-edited cell lines was provided by the Bruce R. Conklin Laboratory at the Gladstone Institute and UCSF. We also thank Sean Palecek, Vilas Menon, and Georg Seelig for their guidance and feedback on gene expression. We thank Natalie DeWitt for her assistance with editing the manuscript text. Julie A. Theriot was supported by funding from the Howard Hughes Medical Institute. We would like to thank the Allen Institute for Cell Science founder, Paul G. Allen, for his vision, encouragement, and support.

AUTHOR CONTRIBUTIONS

Conceptualization, K.A.G., T.G., M.C.H., R.M.D.-M., S.M.R., J.A.T., and R.N.G.; methodology, R.M.D.-M., M.P.V., C.Y., J.C., H.L., K.A.G., T.G., M.C.H., M.F.S., S.M.R., and J.A.T.; software, J.M.B., J.C., G.R.J., M.P.V., M.F.S., H.L., C.Y., R.M.D.-M., and T.G.; formal analysis, T.G., R.M.D.-M., M.P.V., M.F.S., and C.Y.; investigation, K.A.G., T.G., M.C.H., A.M.N., C.Y., R.J.Z., S.Q.D., A.N., H.G.A., and J.L.G.; data curation, R.M.D.-M., T.G., J.M.B., C.Y., and M.P.V.; writing – original draft, K.A.G., T.G., M.C.H., and R.M.D.-M.; writing – review & editing, R.N.G., J.A.T., S.M.R., K.A.G., T.G., M.C.H., R.M.D.-M., and K.R.C.M.; visualization, K.R.C.M., K.A.G., T.G., M.C.H., R.M.D.-M., R.J.Z., and M.P.V.; supervision, R.N.G., J.A.T., S.M.R., N.G., and T.K.; project administration, K.R.C.M., R.N.G., K.A.G., and M.C.H.

DECLARATION OF INTERESTS

The authors declare no competing interests.

Received: May 27, 2020

Revised: December 7, 2020

Accepted: April 30, 2021

Published: May 26, 2021; corrected online June 4, 2021

REFERENCES

- Abbot, E.S. (1916). The causal relations between structure and function in biology. *Am. J. Psychol.* 27, 245–250.
- Ackers-Johnson, M., Tan, W.L.W., and Foo, R.S. (2018). Following hearts, one cell at a time: recent applications of single-cell RNA sequencing to the understanding of heart disease. *Nat. Commun.* 9, 4434.
- Allen Institute for Cell Science (2020). Allen cell explorer. <https://www.allencell.org/>.
- Andrews, T.S., and Hemberg, M. (2018). Identifying cell populations with scRNASeq. *Mol. Aspects Med.* 59, 114–122.
- Bargehr, J., Ong, L.P., Colzani, M., Davaapil, H., Hofsteen, P., Bhandari, S., Gambardella, L., Le Novère, N., Iyer, D., Sampaziotis, F., et al. (2019). Epicardial cells derived from human embryonic stem cells augment cardiomyocyte-driven heart regeneration. *Nat. Biotechnol.* 37, 895–906.
- Bertero, A., Fields, P.A., Ramani, V., Bonora, G., Yardimci, G.G., Reinecke, H., Pabon, L., Noble, W.S., Shendure, J., and Murry, C.E. (2019). Dynamics of genome reorganization during human cardiogenesis reveal an RBM20-dependent splicing factory. *Nat. Commun.* 10, 1538.
- Bottone, M.G., Santin, G., Aredia, F., Bernocchi, G., Pellicciari, C., and Scovassi, A.I. (2013). Morphological features of organelles during apoptosis: an overview. *Cells* 2, 294–305.
- Bouvagnet, P., Neveu, S., Montoya, M., and Leger, J.J. (1987). Development changes in the human cardiac isomyosin distribution: an immunohistochemical study using monoclonal antibodies. *Circ. Res.* 61, 329–336.
- Bray, M.A., Sheehy, S.P., and Parker, K.K. (2008). Sarcomere alignment is regulated by myocyte shape. *Cell Motil. Cytoskeleton* 65, 641–651.
- Brown, J. (2019). Managing manifests and distributing datasets (Zenodo). <https://doi.org/10.5281/zenodo.3382258>.
- Cao, J., Navis, A., Cox, B.D., Dickson, A.L., Gemberling, M., Karra, R., Bagnat, M., and Poss, K.D. (2016). Single epicardial cell transcriptome sequencing identifies caveolin 1 as an essential factor in zebrafish heart regeneration. *Development* 143, 232–243.
- Champion, L., Linder, M.I., and Kutay, U. (2017). Cellular reorganization during mitotic entry. *Trends Cell Biol.* 27, 26–41.
- Chaudhry, F., Isherwood, J., Bawa, T., Patel, D., Gurdziel, K., Lanfear, D.E., Ruden, D.M., and Levy, P.D. (2019). Single-cell RNA sequencing of the cardiovascular system: new looks for old diseases. *Front. Cardiovasc. Med.* 6, 173.
- Chen, J., Ding, L., Viana, M.P., Lee, H., Sluzewski, F., Morris, B., Hendershot, M.C., Yang, R., Mueller, I.A., and Rafelski, S.M. (2020). The allen cell structure segmenter: a new open source toolkit for segmenting 3D intracellular structures fluorescence microscopy images. bioRxiv <https://www.biorxiv.org/content/10.1101/491035v1>.
- Chen, K.H., Boettiger, A.N., Moffitt, J.R., Wang, S., and Zhuang, X. (2015). RNA imaging: Spatially resolved, highly multiplexed RNA profiling in single cells. *Science* 348, aaa6090.
- Chen, L.-C., Papandreou, G., Schroff, F., and Hartwig, A. (2017). Rethinking atrous convolution for semantic image segmentation. arXiv, arXiv:1706.05587.
- Chopra, A., Kutys, M.L., Zhang, K., Polacheck, W.J., Sheng, C.C., Luu, R.J., Eyckmans, J., Hinson, J.T., Seidman, J.G., Seidman, C.E., et al. (2018). Force generation via beta-cardiac myosin, titin, and alpha-actinin drives cardiac sarcomere assembly from cell-matrix adhesions. *Dev. Cell* 44, 87–96.e5.
- Cui, Y., Zheng, Y., Liu, X., Yan, L., Fan, X., Yong, J., Hu, Y., Dong, J., Li, Q., Wu, X., et al. (2019). Single-cell transcriptome analysis maps the developmental track of the human heart. *Cell Rep* 26, 1934–1950.e5.

- DeLaughter, D.M., Bick, A.G., Wakimoto, H., McKean, D., Gorham, J.M., Kathiriya, I.S., Hinson, J.T., Homsy, J., Gray, J., Pu, W., et al. (2016). Single-cell resolution of temporal gene expression during heart development. *Dev. Cell* 39, 480–490.
- Denning, C., Borgdorff, V., Crutchley, J., Firth, K.S., George, V., Kalra, S., Kondrashov, A., Hoang, M.D., Mosqueira, D., Patel, A., et al. (2016). Cardiomyocytes from human pluripotent stem cells: from laboratory curiosity to industrial biomedical platform. *Biochim. Biophys. Acta* 1863, 1728–1748.
- Dunn, K.K., Reichardt, I.M., Simmons, A.D., Jin, G., Floy, M.E., Hoon, K.M., and Palecek, S.P. (2019). Coculture of endothelial cells with human pluripotent stem cell-derived cardiac progenitors reveals a differentiation stage-specific enhancement of cardiomyocyte maturation. *Biotechnol. J.* 14, e1800725.
- Edfors, F., Danielsson, F., Hallström, B.M., Käll, L., Lundberg, E., Pontén, F., Forsström, B., and Uhlén, M. (2016). Gene-specific correlation of RNA and protein levels in human cells and tissues. *Mol. Syst. Biol.* 12, 883.
- Efron, B. (1979). Bootstrap methods: another look at the jackknife. *Ann. Statist.* 7, 1–26.
- Eng, C.-H.L., Lawson, M., Zhu, Q., Dries, R., Koulena, N., Takei, Y., Yun, J., Cronin, C., Karp, C., Yuan, G.-C., and Cai, L. (2019). Transcriptome-scale super-resolved imaging in tissues by RNA seqFISH+. *Nature* 568, 235–239.
- Eschenhagen, T., and Carrier, L. (2019). Cardiomyopathy phenotypes in human-induced pluripotent stem cell-derived cardiomyocytes—a systematic review. *Pflügers Arch* 471, 755–768.
- Etienne-Manneville, S. (2008). Polarity proteins in migration and invasion. *Oncogene* 27, 6970–6980.
- Fenix, A.M., Neininger, A.C., Taneja, N., Hyde, K., Visetsouk, M.R., Garde, R.J., Liu, B., Nixon, B.R., Manalo, A.E., Becker, J.R., et al. (2018). Muscle-specific stress fibers give rise to sarcomeres in cardiomyocytes. *eLife* 7, e42144.
- Friedman, C.E., Nguyen, Q., Lukowski, S.W., Helfer, A., Chiu, H.S., Miklas, J., Levy, S., Suo, S., Han, J.-D.J., Osteil, P., et al. (2018). Single-cell transcriptomic analysis of cardiac differentiation from human PSCs reveals HOPX-dependent cardiomyocyte maturation. *Cell Stem Cell* 23, 586–598.e8.
- Genshaft, A.S., Li, S., Gallant, C.J., Darmanis, S., Prakadan, S.M., Ziegler, C.G., Lundberg, M., Fredriksson, S., Hong, J., Regev, A., et al. (2016). Multiplexed, targeted profiling of single-cell proteomes and transcriptomes in a single reaction. *Genome Biol* 17, 188.
- Goltsev, Y., Samusik, N., Kennedy-Darling, J., Bhave, S., Hale, M., Vazquez, G., Black, S., and Nolan, G.P. (2018). Deep profiling of mouse splenic architecture with CODEX multiplexed imaging. *Cell* 174, 968–981.e15.
- Gorza, L., Mercadier, J.J., Schwartz, K., Thornell, L.E., Sartore, S., and Schiaffino, S. (1984). Myosin types in the human heart. An immunofluorescence study of normal and hypertrophied atrial and ventricular myocardium. *Circ. Res.* 54, 694–702.
- Grancharova, T., Gerbin, K.A., Rosenberg, A.B., Rocco, C.M., Arakaki, J., DeLizzo, C., Dinh, S.Q., Donovan-Maiye, R., Hirano, M., Nelson, A., et al. (2021). A comprehensive analysis of gene expression changes in a high replicate and open-source dataset of differentiating hiPSC-derived cardiomyocytes. *bioRxiv* <https://www.biorxiv.org/content/10.1101/2021.04.22.441027v1>.
- Gut, G., Herrmann, M.D., and Pelkmans, L. (2018). Multiplexed protein maps link subcellular organization to cellular states. *Science* 361, eaar7042.
- Haralick, R.M. (1979). Statistical and structural approaches to texture. *Proc. IEEE* 67, 786–804.
- Heimberg, G., Bhatnagar, R., El-Samad, H., and Thomson, M. (2016). Low dimensionality in gene expression data enables the accurate extraction of transcriptional programs from shallow sequencing. *Cell Syst* 2, 239–250.
- Huxley, A.F., and Niedergerke, R. (1954). Structural changes in muscle during contraction; interference microscopy of living muscle fibres. *Nature* 173, 971–973.
- Huxley, H., and Hanson, J. (1954). Changes in the cross-striations of muscle during contraction and stretch and their structural interpretation. *Nature* 173, 973–976.
- Judge, L.M., Perez-Bermejo, J.A., Truong, A., Ribeiro, A.J., Yoo, J.C., Jensen, C.L., Mandegar, M.A., Huebsch, N., Kaake, R.M., So, P.-L., et al. (2017). A BAG3 chaperone complex maintains cardiomyocyte function during proteotoxic stress. *JCI Insight* 2, e94623.
- Kamakura, T., Makiyama, T., Sasaki, K., Yoshida, Y., Wuriyanghai, Y., Chen, J., Hattori, T., Ohno, S., Kita, T., Horie, M., et al. (2013). Ultrastructural maturation of human-induced pluripotent stem cell-derived cardiomyocytes in a long-term culture. *Circ. J.* 77, 1307–1314.
- Kamentsky, L., Jones, T.R., Fraser, A., Bray, M.A., Logan, D.J., Madden, K.L., Ljosa, V., Rueden, C., Eliceiri, K.W., and Carpenter, A.E. (2011). Improved structure, function and compatibility for CellProfiler: modular high-throughput image analysis software. *Bioinformatics* 27, 1179–1180.
- Kandel, E.R., Schwartz, J.H., Jessell, T.M., Siegelbaum, S.A., and Hudspeth, A.J. (2012). *Principles of Neural Science*, Fifth Edition (McGraw-Hill Education).
- Karbassi, E., Fenix, A., Marchiano, S., Muraoka, N., Nakamura, K., Yang, X., and Murry, C.E. (2020). Cardiomyocyte maturation: advances in knowledge and implications for regenerative medicine. *Nat. Rev. Cardiol.* 17, 341–359.
- Kasahara, H., Ueyama, T., Wakimoto, H., Liu, M.K., Maguire, C.T., Converso, K.L., Kang, P.M., Manning, W.J., Lawitts, J., Paul, D.L., et al. (2003). Nkx2.5 homeoprotein regulates expression of Gap junction protein connexin 43 and sarcomere organization in postnatal cardiomyocytes. *J. Mol. Cell. Cardiol.* 35, 243–256.
- Kokkinopoulos, I., Ishida, H., Saba, R., Ruchaya, P., Cabrera, C., Strubig, M., Barnes, M., Terry, A., Kaneko, M., Shintani, Y., et al. (2015). Single-cell expression profiling reveals a dynamic state of cardiac precursor cells in the early mouse embryo. *PLoS One* 10, e0140831.
- Kubalak, S.W., Miller-Hance, W.C., O'Brien, T.X., Dyson, E., and Chien, K.R. (1994). Chamber specification of atrial myosin light chain-2 expression precedes septation during murine cardiogenesis. *J. Biol. Chem.* 269, 16961–16970.
- Lee, J.H., Daugherty, E.R., Scheiman, J., Kalhor, R., Ferrante, T.C., Terry, R., Turczyk, B.M., Yang, J.L., Lee, H.S., Aach, J., et al. (2015). Fluorescent in situ sequencing (FISSEQ) of RNA for gene expression profiling in intact cells and tissues. *Nat. Protoc.* 10, 442–458.
- Lescroart, F., Wang, X., Lin, X., Swedlund, B., Gargouri, S., Sánchez-Dáñez, A., Moignard, V., Dubois, C., Paulissen, C., Kinston, S., et al. (2018). Defining the earliest step of cardiovascular lineage segregation by single-cell RNA-seq. *Science* 359, 1177–1181.
- Li, G., Xu, A., Sim, S., Priest, J.R., Tian, X., Khan, T., Quertermous, T., Zhou, B., Tsao, P.S., Quake, S.R., and Wu, S.M. (2016). Transcriptomic profiling maps anatomically patterned subpopulations among single embryonic cardiac cells. *Dev. Cell* 39, 491–507.
- Lian, X., Hsiao, C., Wilson, G., Zhu, K., Hazeltine, L.B., Azarin, S.M., Raval, K.K., Zhang, J., Kamp, T.J., and Palecek, S.P. (2012). Robust cardiomyocyte differentiation from human pluripotent stem cells via temporal modulation of canonical Wnt signaling. *Proc. Natl. Acad. Sci. USA* 109, E1848–E1857.
- Lian, X., Zhang, J., Azarin, S.M., Zhu, K., Hazeltine, L.B., Bao, X., Hsiao, C., Kamp, T.J., and Palecek, S.P. (2013). Directed cardiomyocyte differentiation from human pluripotent stem cells by modulating Wnt/beta-catenin signaling under fully defined conditions. *Nat. Protoc.* 8, 162–175.
- Liu, J., Huang, Y., Singh, R., Vert, J.-P., and Noble, W.S. (2019). Jointly embedding multiple single-cell omics measurements. *bioRxiv* <https://www.biorxiv.org/content/10.1101/644310v1>.
- Liu, Y.W., Chen, B., Yang, X., Fugate, J.A., Kalucki, F.A., Futakuchi-Tsuchida, A., Couture, L., Vogel, K.W., Astley, C.A., Baldessari, A., et al. (2018). Human embryonic stem cell-derived cardiomyocytes restore function in infarcted hearts of non-human primates. *Nat. Biotechnol.* 36, 597–605.
- Lundberg, E., Fagerberg, L., Klevebring, D., Matic, I., Geiger, T., Cox, J., Algenäs, C., Lundeberg, J., Mann, M., and Uhlen, M. (2010). Defining the transcriptome and proteome in three functionally different human cell lines. *Mol. Syst. Biol.* 6, 450.
- Lundy, S.D., Zhu, W.Z., Regnier, M., and Laflamme, M.A. (2013). Structural and functional maturation of cardiomyocytes derived from human pluripotent stem cells. *Stem Cells Dev* 22, 1991–2002.

- Luther, P.K. (2009). The vertebrate muscle Z-disc: sarcomere anchor for structure and signalling. *J. Muscle Res. Cell Motil.* 30, 171–185.
- MacLennan, D.H., Brandl, C.J., Korczak, B., and Green, N.M. (1985). Amino-acid sequence of a Ca^{2+} + Mg^{2+} -dependent ATPase from rabbit muscle sarcoplasmic reticulum, deduced from its complementary DNA sequence. *Nature* 316, 696–700.
- Mann, H.B., and Whitney, D.R. (1947). On a test of whether one of two random variables is stochastically larger than the other. *Ann. Math. Statist.* 18, 50–60.
- Mason, P., Bayol, S., and Loughna, P.T. (1999). The novel sarcomeric protein telethonin exhibits developmental and functional regulation. *Biochem. Biophys. Res. Commun.* 257, 699–703.
- McKinney, W. (2010). Data structures for statistical computing in python. Proceedings of the 9th python in science conference, 51–56.
- McQuin, C., Goodman, A., Chernyshev, V., Kamentsky, L., Cimini, B.A., Karhohs, K.W., Doan, M., Ding, L., Rafelski, S.M., Thirstrup, D., et al. (2018). CellProfiler 3.0: next-generation image processing for biology. *PLoS Biol* 16, e2005970.
- Morris, T.A., Naik, J., Fibben, K.S., Kong, X., Kiyono, T., Yokomori, K., and Grosberg, A. (2020). Striated myocyte structural integrity: automated analysis of sarcomeric z-discs. *PLOS Comput. Biol.* 16, e1007676.
- Napari contributors (2019). Napari: a multi-dimensional image viewer for python. <https://chanzuckerberg.com/napari-a-multi-dimensional-image-viewer-for-python/>.
- Nusinow, D.P., Szpyt, J., Ghandi, M., Rose, C.M., McDonald, E.R., 3rd, Kalocsay, M., Jané-Valbuena, J., Gelfand, E., Schweppe, D.K., Jedrychowski, M., et al. (2020). Quantitative proteomics of the cancer cell line encyclopedia. *Cell* 180, 387–402.e16.
- Oliphant, T.E. (2006). A Guide to NumPy (Trelgol Publishing).
- Ophüls, W. (1906). The relation of anatomic structure to function. *Proc. Soc. Exp. Biol. Med.* 4, 138–139.
- Paik, D.T., Cho, S., Tian, L., Chang, H.Y., and Wu, J.C. (2020). Single-cell RNA sequencing in cardiovascular development, disease and medicine. *Nat. Rev. Cardiol.* 17, 457–473.
- Palpant, N.J., Pabon, L., Friedman, C.E., Roberts, M., Hadland, B., Zaunbrecher, R.J., Bernstein, I., Zheng, Y., and Murry, C.E. (2017). Generating high-purity cardiac and endothelial derivatives from patterned mesoderm using human pluripotent stem cells. *Nat. Protoc.* 12, 15–31.
- Pasqualini, F.S., Sheehy, S.P., Agarwal, A., Aratyn-Schaus, Y., and Parker, K.K. (2015). Structural phenotyping of stem cell-derived cardiomyocytes. *Stem Cell Rep* 4, 340–347.
- Pedregosa, F., Varoquaux, G., Gramfort, A., Michel, V., Thirion, B., Grisel, O., Blondel, M., Prettenhofer, P., Weiss, R., Dubourg, V., et al. (2011). Scikit-learn: machine learning in python. *J. Mach. Learn. Res.* 12, 2825–2830.
- Pervolaraki, E., Dachtler, J., Anderson, R.A., and Holden, A.V. (2018). The developmental transcriptome of the human heart. *Sci. Rep.* 8, 15362.
- Peterson, V.M., Zhang, K.X., Kumar, N., Wong, J., Li, L., Wilson, D.C., Moore, R., McClanahan, T.K., Sadekova, S., and Klappenebach, J.A. (2017). Multiplexed quantification of proteins and transcripts in single cells. *Nat. Biotechnol.* 35, 936–939.
- Pioneer, J.M., Racca, A.W., Klaiman, J.M., Yang, K.-C., Guan, X., Pabon, L., Muskeli, V., Zaunbrecher, R., Macadangdang, J., Jeong, M.Y., et al. (2016). Isolation and mechanical measurements of myofibrils from human induced pluripotent stem cell-derived cardiomyocytes. *Stem Cell Rep* 6, 885–896.
- Popovic, D., Koch, B., Kueblbeck, M., Ellenberg, J., and Pelkmans, L. (2018). Multivariate control of transcript to protein variability in single mammalian cells. *Cell Syst* 7, 398–411.e6.
- Qian, L., Berry, E.C., Fu, J.D., Ieda, M., and Srivastava, D. (2013). Reprogramming of mouse fibroblasts into cardiomyocyte-like cells in vitro. *Nat. Protoc.* 8, 1204–1215.
- Racca, A.W., Klaiman, J.M., Pioneer, J.M., Cheng, Y., Beck, A.E., Moussavi-Harami, F., Bamshad, M.J., and Regnier, M. (2016). Contractile properties of developing human fetal cardiac muscle. *J. Physiol.* 594, 437–452.
- Redd, M.A., Zeinstra, N., Qin, W., Wei, W., Martinson, A., Wang, Y., Wang, R.K., Murry, C.E., and Zheng, Y. (2019). Patterned human microvascular grafts enable rapid vascularization and increase perfusion in infarcted rat hearts. *Nat. Commun.* 10, 584.
- Reiser, P.J., Portman, M.A., Ning, X.H., and Schomisch Moravec, C. (2001). Human cardiac myosin heavy chain isoforms in fetal and failing adult atria and ventricles. *Am. J. Physiol. Heart Circ. Physiol.* 280, H1814–H1820.
- Roberts, B., Haupt, A., Tucker, A., Grancharova, T., Arakaki, J., Fuqua, M.A., Nelson, A., Hookway, C., Ludmann, S.A., Mueller, I.A., et al. (2017). Systematic gene tagging using CRISPR/Cas9 in human stem cells to illuminate cell organization. *Mol. Biol. Cell* 28, 2854–2874.
- Roberts, B., Hendershot, M.C., Arakaki, J., Gerbin, K.A., Malik, H., Nelson, A., Gehring, J., Hookway, C., Ludmann, S.A., Yang, R., et al. (2019). Fluorescent gene tagging of transcriptionally silent genes in hiPSCs. *Stem Cell Rep* 12, 1145–1158.
- Rodriguez, M.L., Graham, B.T., Pabon, L.M., Han, S.J., Murry, C.E., and Sniadecki, N.J. (2014). Measuring the contractile forces of human induced pluripotent stem cell-derived cardiomyocytes with arrays of microposts. *J. Biomech. Eng.* 136, 051005.
- Ronaldson-Bouchard, K., Ma, S.P., Yeager, K., Chen, T., Song, L., Sirabella, D., Morikawa, K., Teles, D., Yazawa, M., and Vunjak-Novakovic, G. (2018). Advanced maturation of human cardiac tissue grown from pluripotent stem cells. *Nature* 556, 239–243.
- Sacchetto, C., Vitiello, L., de Windt, L.J., Rampazzo, A., and Calore, M. (2020). Modeling cardiovascular diseases with hiPSC-derived cardiomyocytes in 2D and 3-D cultures. *Int. J. Mol. Sci.* 21, 3404.
- Sanger, J.W., Kang, S., Siebrands, C.C., Freeman, N., Du, A., Wang, J., Stout, A.L., and Sanger, J.M. (2005). How to build a myofibril. *J. Muscle Res. Cell Motil.* 26, 343–354.
- Schindelin, J., Arganda-Carreras, I., Frise, E., Kaynig, V., Longair, M., Pietzsch, T., Preibisch, S., Rueden, C., Saalfeld, S., Schmid, B., et al. (2012). Fiji: an open-source platform for biological-image analysis. *Nat. Methods* 9, 676–682.
- Schulz, D., Zanotelli, V.R.T., Fischer, J.R., Schapiro, D., Engler, S., Lun, X.K., Jackson, H.W., and Bodenmiller, B. (2018). Simultaneous multiplexed imaging of mRNA and proteins with subcellular resolution in breast cancer tissue samples by mass cytometry. *Cell Syst* 6, 25–36.e5.
- Sereti, K.I., Nguyen, N.B., Kamran, P., Zhao, P., Ranjbarvaziri, S., Park, S., Sabri, S., Engel, J.L., Sung, K., Kulkarni, R.P., et al. (2018). Analysis of cardiomyocyte clonal expansion during mouse heart development and injury. *Nat. Commun.* 9, 754.
- Sheehy, S.P., Pasqualini, F., Grosberg, A., Park, S.J., Aratyn-Schaus, Y., and Parker, K.K. (2014). Quality metrics for stem cell-derived cardiac myocytes. *Stem Cell Rep* 2, 282–294.
- Shekhar, K., and Menon, V. (2019). Identification of cell types from single-cell transcriptomic data. *Methods Mol. Biol.* 1935, 45–77.
- Snir, M., Kehat, I., Gepstein, A., Coleman, R., Itskovitz-Eldor, J., Livne, E., and Gepstein, L. (2003). Assessment of the ultrastructural and proliferative properties of human embryonic stem cell-derived cardiomyocytes. *Am. J. Physiol. Heart Circ. Physiol.* 285, H2355–H2363.
- Spearman, C. (2010). The proof and measurement of association between two things. *Int. J. Epidemiol.* 39, 1137–1150.
- Suryawanshi, H., Clancy, R., Morozov, P., Halushka, M.K., Buyon, J.P., and Tuschl, T. (2020). Cell atlas of the foetal human heart and implications for auto-immune-mediated congenital heart block. *Cardiovasc. Res.* 116, 1446–1457.
- Sutcliffe, M.D., Tan, P.M., Fernandez-Perez, A., Nam, Y.J., Munshi, N.V., and Saucerman, J.J. (2018). High content analysis identifies unique morphological features of reprogrammed cardiomyocytes. *Sci. Rep.* 8, 1258.
- Toepfer, C.N., Sharma, A., Cicconet, M., Garfinkel, A.C., Mücke, M., Neyazi, M., Willcox, J.A.L., Agarwal, R., Schmid, M., Rao, J., et al. (2019). SarcTrack. *Circ. Res.* 124, 1172–1183.
- Vallat, R. (2018). Pingouin: statistics in Python. *J. Open Source Software* 3, 1026.

- Van Meer, B.J., Tertoolen, L.G., and Mummery, C.L. (2016). Concise review: measuring physiological responses of human pluripotent stem cell derived cardiomyocytes to drugs and disease. *Stem Cells* 34, 2008–2015.
- Van Rossum, G., and Drake, F.L., Jr. (2009). Python 3 Reference Manual (CreateSpace).
- VanderPlas, J., Granger, B., Heer, J., Moritz, D., Wongsuphasawat, K., Satyanarayan, A., Lees, E., Timofeev, I., Welsh, B., and Sievert, S. (2018). Altair: interactive statistical visualizations for python. *J. Open Source Software* 3, 1057.
- Veerman, C.C., Kosmidis, G., Mummery, C.L., Casini, S., Verkerk, A.O., and Bellin, M. (2015). Immaturity of human stem-cell-derived cardiomyocytes in culture: fatal flaw or soluble problem? *Stem Cells Dev* 24, 1035–1052.
- Virtanen, P., Gommers, R., Oliphant, T.E., Haberland, M., Reddy, T., Cournapeau, D., Burovski, E., Peterson, P., Weckesser, W., Bright, J., et al. (2020). SciPy 1.0: fundamental algorithms for scientific computing in Python. *Nat. Methods* 17, 261–272.
- Wang, G., Moffitt, J.R., and Zhuang, X. (2018). Multiplexed imaging of high-density libraries of RNAs with MERFISH and expansion microscopy. *Sci. Rep.* 8, 4847.
- Waskom, M., Botvinnik, O., Ostblom, J., Lukauskas, S., Hobson, P., MaozGelbart, Gemperline, D.C., Augspurger, T., Halchenko, Y., Cole, J.B., et al. (2020). mwaskom/seaborn: v0.10.0 (January 2020) (Zenodo). <https://zenodo.org/record/3629446#.YJZe6LUzbIU>.
- Wasserman, L. (2006). All of Nonparametric Statistics, First Edition (Springer-Verlag).
- Weber, N., Kowalski, K., Holler, T., Radocaj, A., Fischer, M., Thiemann, S., de la Roche, J., Schwanke, K., Piep, B., Peschel, N., et al. (2020). Advanced single-cell mapping reveals that in hESC cardiomyocytes contraction kinetics and action potential are independent of myosin isoform. *Stem Cell Rep* 14, 788–802.
- Weber, N., Schwanke, K., Greten, S., Wendland, M., Iorga, B., Fischer, M., Geers-Knörr, C., Hegermann, J., Wrede, C., Fiedler, J., et al. (2016). Stiff matrix induces switch to pure β -cardiac myosin heavy chain expression in human ESC-derived cardiomyocytes. *Basic Res. Cardiol.* 111, 68.
- Wolf, F.A., Angerer, P., and Theis, F.J. (2018). SCANPY: large-scale single-cell gene expression data analysis. *Genome Biol* 19, 15.
- Xiao, Y., Hill, M.C., Zhang, M., Martin, T.J., Morikawa, Y., Wang, S., Moise, A.R., Wythe, J.D., and Martin, J.F. (2018). Hippo signaling plays an essential role in cell state transitions during cardiac fibroblast development. *Dev. Cell* 45, 153–169.e6.
- Xu, X.Q., Soo, S.Y., Sun, W., and Zweigerdt, R. (2009). Global expression profile of highly enriched cardiomyocytes derived from human embryonic stem cells. *Stem Cells* 27, 2163–2174.
- Yang, X., Pabon, L., and Murry, C.E. (2014). Engineering adolescence: maturation of human pluripotent stem cell-derived cardiomyocytes. *Circ. Res.* 114, 511–523.

STAR★METHODS

KEY RESOURCES TABLE

REAGENT or RESOURCE	SOURCE	IDENTIFIER
Antibodies		
anti-cardiac Troponin T AlexaFluor® 647	BD Biosciences	Cat# 565744; RRID: AB_2739341
mlgG1, k AF647 isotype control	BD Biosciences	Cat# 565571; RRID: AB_2687590
anti-cardiac Troponin T, rabbit polyclonal	Abcam	Cat# ab45932; RRID: AB_956386
anti-beta myosin heavy chain, supernatant	Developmental Studies Hybridoma Bank (DSHB)	Cat# A4.951; RRID: AB_528385
Anti-alpha myosin heavy chain	R&D Systems	Cat# MAB8979
Anti-titin, n-term, z-disk	Myomedix	Cat # TTN-1
Anti-myosin light chain 2a	Synaptic Systems	Cat# 311 011; RRID: AB_887737
Chemicals, peptides, and recombinant proteins		
mTESR media (basal media plus supplement)	STEMCELL Technologies	85850
Growth Factor Reduced (GFR) Matrigel®	Corning	354230
ROCK inhibitor (Y-27632)	STEMCELL Technologies	72308
RPMI-1640	Gibco Life Technologies	A10491-01
B27 supplement (50x), serum free	Gibco Life Technologies	12587010
B-27 Supplement, minus insulin	Gibco Life Technologies	A1895601
StemPro Accutase	Gibco Life Technologies	A11105-01
CHIR99021	Cayman Chemical Company	13122
IWP 2	R&D Systems	3533
Critical commercial assays		
HCR v3.0 Bundle RNA FISH assay	Molecular Instruments	https://www.molecularinstruments.com/hcr-v3
BMPER probe set	Molecular Instruments	3112/C279
CNTN5 probe set	Molecular Instruments	3112/C281
COL2A1 probe set	Molecular Instruments	3178/C651
H19 probe set	Molecular Instruments	PRA737
MYH6 probe set	Molecular Instruments	2674/B797
MYH7 probe set	Molecular Instruments	2674/B805
PLN probe set	Molecular Instruments	3178/C653
PRSS35 probe set	Molecular Instruments	3178/C659
VCAN probe set	Molecular Instruments	3112/C277
ACTN2 probe set	Molecular Instruments	PRB749
ATP2A2 probe set	Molecular Instruments	PRB751
BAG3 probe set	Molecular Instruments	PRB755
MYL7 probe set	Molecular Instruments	3178/C665
NKX2-5 probe set	Molecular Instruments	2674/B803
TCAP probe set	Molecular Instruments	PRB754
TTN probe set	Molecular Instruments	PRB752
HPRT1 probe set	Molecular Instruments	3112/C275
MEF2C probe set	Molecular Instruments	PRA732
Deposited data		
All data used are available in the Allen Cell open resource data package	Allen Institute	https://open.quiltdata.com/b/allencell/packages/aics/integrated_transcriptomics_structural_organization_hipsc_cm

(Continued on next page)

Continued

REAGENT or RESOURCE	SOURCE	IDENTIFIER
Experimental models: Cell lines		
Human: unedited parental line AICS-00 WTC (used to generate the AICS-0075 cell line)	Allen Cell Collection	allencell.org/cell-catalog
Human: AICS-0075 cl.85 ACTN2-mEGFP	Allen Cell Collection	allencell.org/cell-catalog
Software and algorithms		
CellProfiler (version 3.1.8)	Kamentsky et al., 2011	https://www.cellprofiler.org
Fiji	Schindelin et al., 2012	https://fiji.sc/
FlowJo software V. 10.2	Treestar	https://www.flowjo.com/solutions/flowjo
Allen Cell Structure Segmenter (version 0.1.12)	Chen et al., 2020	https://github.com/AllenCell/aics-segmentation
Python (version 3.7)	Van Rossum and Drake, 2009	https://www.python.org
Numpy 1.18.2	Oliphant, 2006	https://numpy.org/
Scipy 1.4.1	Virtanen et al., 2020	https://www.scipy.org
Pandas 1.0.3	McKinney, 2010	https://pandas.pydata.org
scikit-learn 0.22.2	Pedregosa et al., 2011	https://scikit-learn.org
AnnData 0.7.1	Wolf et al., 2018	https://anntadata.readthedocs.io
Pingouin 0.3.3	Vallat, 2018	https://pingouin-stats.org
Altair 4.0.1	VanderPlas et al., 2018	https://altair-viz.github.io
Seaborn 0.10.0	Waskom et al., 2020	https://seaborn.pydata.org
quilt3distribute 0.1.3	Brown, 2019	https://github.com/AllenCellModeling/quilt3distribute
Napari (version 0.1.4)	Napari contributors, 2019	https://github.com/napari/napari
Pytorch (version 1.3.0)	Paszke et al., 2019	https://pytorch.org
Torchvision (version 0.4.1)	Python package	https://pytorch.org
Pillow (version 6.2.0)	Python package	https://pillow.readthedocs.io
Scikit-image (version 0.15.0)	Van der Walt et al., 2014	https://scikit-image.org/
DeepLabV3	Chen et al., 2017	https://github.com/tensorflow/models/tree/master/research/deeplab
Other		
3i spinning-disk microscope, CSU-W1 spinning disc	3i	https://www.intelligent-imaging.com/spinning-disk-confocal
CytoFLEX S	Beckman Coulter	https://www.beckman.com/flow-cytometry/instruments/cytoflex-s

RESOURCE AVAILABILITY

Lead contact

Further information and requests for resources and reagents should be directed to and will be fulfilled by the Lead Contact, Ruwanthi N. Gunawardane (rug@alleninstitute.org).

Materials availability

This study did not generate new materials. The tagged hiPSC line used in this study (AICS-0075 cl.85) can be obtained through the Allen Cell Catalog (www.allencell.org/cell-catalog). The donor plasmid used to derive the cell line described in this study is available in Addgene, AICSDP-63:ACTN2-mEGFP (ID: 124607).

Data and code availability

Source Data: Source data is available as a publicly accessible Quilt package: https://open.quiltdata.com/b/allencell/packages/aics/integrated_transcriptomics_structural_organization_hipsc_cm

Code: All original code for performing data analysis is publicly available through the Allen Cell Modeling GitHub repository accessible at: https://github.com/AllenCellModeling/fish_morphology_code

Manual annotation was performed using Napari, accessible at: <https://github.com/Napari/napari>, and <https://github.com/AllenCellModeling/napari-annotation-tools>

Scripts: The scripts used to generate the figures reported in this paper are available at: https://github.com/AllenCellModeling/fish_morphology_manuscript_notebooks/tree/master/notebooks

Additional information: Any additional information required to reproduce this work is available from the Lead Contact.

EXPERIMENTAL MODEL AND SUBJECT DETAILS

Cell lines and plasmids

All work with human induced pluripotent stem cell (hiPSC) lines was approved by internal oversight committees and was conducted in accordance with NIH, NAS, and ISSCR guidelines. The genetically edited hiPSC line used in this study, AICS-0075 cl.85 (ACTN2-mEGFP), was generated as described previously (Roberts et al., 2019) and can be obtained through the Allen Cell Collection (Allen Institute for Cell Science, 2020). The donor plasmid used to generate this cell line is AICSDP-63:ACTN2-mEGFP (ID: 124607) and can be obtained through Addgene (https://www.addgene.org/The_Allen_Institute_for_Cell_Science/).

METHOD DETAILS

Human induced pluripotent stem cell culture

hiPSCs were maintained in mTeSR1 (Stem Cell Technologies #85850) supplemented with 1% penicillin/streptomycin (P/S) (Gibco #15070063) on plates coated with growth factor reduced matrigel (Corning #354230). hiPSCs were passaged as single cells after reaching 70-85% confluence every 3-4 days using Accutase (Gibco #A11105-01) and re plated in mTeSR1 supplemented with 1% P/S and 10 µM ROCK inhibitor (Y-27632, Stem Cell Technologies #72308). A detailed, step by step protocol is available at the Allen Cell Explorer (www.allencell.org/methods-for-cells-in-the-lab, SOP: WTC culture v1.7.pdf, Allen Institute for Cell Science, 2020).

Directed cardiomyocyte differentiation

Cardiomyocytes were generated from hiPSCs using a previously reported small molecule differentiation method (Lian et al., 2012, 2013) with some modifications (Roberts et al., 2019), schematic in Figure S1B. Briefly, hiPSCs were dissociated into a single cell suspension using Accutase and seeded into matrigel-coated 6 well-plates at 125k - 350k cells per well in mTeSR1 supplemented with 1% P/S and 10 µM ROCK inhibitor (denoted as Day -3). Cells were fed daily with mTeSR1 media for 2 days, and on the third day (Day 0) differentiation was initiated with the addition of RPMI-1640 (Invitrogen #A10491-01) supplemented with B27 without insulin (Invitrogen #A1895601) and 7.5 µM CHIR99021 (Cayman Chemical #13122). At 48 hours (Day 2) media was replaced with RPMI-1640 supplemented with B27 without insulin and 7.5 µM IWP2 (R&D Systems #3533). After an additional 48 hours (Day 4), media was replaced with RPMI-1640 supplemented with B27-without insulin, and replaced every 2-3 days thereafter (starting on Day 6) with RPMI-1640 supplemented with B27 containing insulin (Invitrogen #12587010) and 1% P/S. Spontaneous beating was generally observed between Days 7-12. Please note that we recently updated our protocols and now recommend the use of RPMI-1640 (Invitrogen #11875-093) and B27 supplement (Gibco #17504044) for cardiac differentiation. A detailed, step by step protocol is available at the Allen Cell Explorer (www.allencell.org/methods-for-cells-in-the-lab, SOP: Cardiomyocyte differentiation methods_v1.2.pdf, Allen Institute for Cell Science, 2020).

Single cell dissociation for replating onto glass

Wells of differentiated cardiomyocytes were visually inspected at Day 12 for successful differentiation on the basis of a high percentage of cardiomyocytes, spontaneous beating, and morphology; wells that passed these criteria were collected for downstream analysis (n= 1 - 4 wells of a 6 well-plate chosen for replating per experiment, see Table S1). To dissociate cardiomyocytes into single cells, wells were first washed with 1X DPBS (Gibco #14190-144) and incubated with pre-warmed 2X TrypLE Select (Gibco #A12177) diluted in Versene (Gibco #15040-066) for 8-10 minutes at 37°C. Monolayers were gently dissociated into a single cell suspension using a P1000 micropipette and added to 5 mL of RPMI-1640 containing B27 supplement, 1% P/S, 10 µM ROCK inhibitor and 200 U/mL DNase I (Millipore Sigma #260913-10MU) (resuspension media). Wells were washed twice with an additional 1 mL of resuspension media, and the cell suspension was centrifuged at 300 x g for 5 minutes at 4°C. Cells were gently resuspended in 5 mL of resuspension media and counted twice on a hemocytometer and averaged to obtain a total cell count for each sample.

Flow cytometry of samples for replating

At the time of single cell dissociation as described above, an aliquot was taken from each cell sample for cardiac troponin T (cTnT) analysis by flow cytometry as previously described (Roberts et al., 2017). Briefly, aliquots were fixed in 4% paraformaldehyde (Electron Microscopy Sciences #15710) in DPBS for 10 min. Fixed samples were stained in BD Perm/Wash™ buffer (BD Biosciences #512091KZ) containing anti-cardiac troponin T AlexaFluor® 647 (BD Biosciences #565744) or equal mass of AF647 IgG1 κ isotype control (BD Biosciences #565571) for 30 min followed by resuspension in 5% FBS (Gibco #10437028) in DPBS with 2 µg/mL DAPI before processing and data acquisition on a CytoFLEX S (Beckman Coulter). Analysis was conducted using FlowJo software V. 10.2 (Treestar).

Replating cardiomyocytes for imaging and RNA FISH

After cardiomyocyte differentiation, cells were dissociated into single cells at D12 (described in “Single cell dissociation for replating on glass” section), and flow cytometry was performed on a subset of cells for cardiac troponin T analysis as described in the “Flow

cytometry of samples for replating” section above. Prior to cell plating, glass bottom multiwell plates (24-well, Cellvis P24-1.5H-N) were treated with 0.5 M glacial acetic acid (Fisher Scientific #BP1185-500) at RT for 20–60 min and washed once with sterile milliQ (MQ) water. Wells were then treated with 0.1% PEI (Sigma Aldrich #408727-100ML) solution in sterile MQ water for 16–72 h at 4°C, rinsed once with DPBS and once with sterile MQ water. Finally, wells were incubated overnight at 4°C with 25 µg/mL natural mouse laminin (Gibco #23017-015) diluted in sterile MQ water. Laminin solution was removed immediately prior to replating; cells were seeded at a density of 35,000 to 50,000 cells per well (24-well plate) in RPMI-1640 supplemented with B27 containing insulin, 1% P/S and 10 µM ROCK inhibitor. Media was changed after 24 hrs, and cells were fed with RPMI-1640 supplemented with B27 containing insulin and 1% P/S every 2–3 days until fixation. Cells were fixed at time points indicated in text for RNA FISH and imaging of alpha-actinin-2-mEGFP. Reported time points in the figures and text reflect the time since the initiation of differentiation (D0) and include samples within a 2-day period; i.e., D18 includes D18-19, D25 includes D25-26, and D32 includes D32-33 samples. For two experiments, one replate contributed to matched time points at D18, D25, and D32 and were used for both RNA FISH and live imaging studies, while two experiments had re plates contributing to only RNA FISH studies, and three experiments had re plates used for only live imaging studies. All differentiation and sample metadata can be found in **Table S1**. For fixed samples (see “[RNA FISH using HCR v3.0](#)” section below), media was removed, and wells were washed twice with RNase-free PBS. Cells were fixed for 10 min at RT in a 4% paraformaldehyde solution (Electron Microscopy Sciences #15710), and then washed once more with RNase-free PBS. PBS was removed and replaced with 70% ethanol; fixed plates were wrapped with parafilm and stored at -20°C until RNA hybridization was performed.

Cardiomyocyte immunolabeling for imaging

Cells were fixed with 4% paraformaldehyde in PBS with 0.4% Triton X-100 (EMD Millipore #TX1568-3) for 10 min at room temperature and blocked with 1.5% normal goat serum (Vector Laboratories #S-1000-20) with 0.4% Triton X-100 in PBS (blocking solution) for 1–3 h at room temperature. Primary antibodies (anti-beta myosin heavy chain, DSHB, A4.951 supernatant, 1:5.3 and anti-alpha myosin heavy chain, R&D Systems, MAB8979, 1:133.3) were diluted in blocking solution and incubated at 4°C overnight. Secondary antibodies were diluted in blocking solution at 1:500 to 1:1,000 for 2–3 h at room temperature. DAPI (NucBlue Fixed Cell ReadyProbes Reagent; Thermo Fisher R37606) was applied for 5 min at room temperature.

WGA staining of live cardiomyocytes for imaging

Wheat germ agglutinin (CF®633 WGA, Biotium, #29024) and Nuclear Violet™ LCS1 (AAT Bioquest #17543) stock solutions were diluted according to manufacturer’s instructions to make a 5 µg/ml WGA and 0.67 µM Nuclear Violet™ staining solution in phenol red-free RPMI-1640 (Gibco #11835030) supplemented with B27 containing insulin. Cells were incubated for 10 minutes in staining solution at 37°C and 5% CO₂, then were washed once with phenol red-free RPMI-1640 supplemented with B27 containing insulin. Cells were imaged in phenol red-free RPMI-1640 supplemented with B27 containing insulin plus 20 mM 2,3-butanedione 2-monoxime (BDM, Abcam #ab120616) to inhibit spontaneous beating. Imaging was completed within two hours of BDM and dye application.

RNA FISH using HCR v3.0

RNA FISH was performed using HCR v3.0, following the HCR v3.0 protocol for “Mammalian cells on a slide” with modifications to adapt for samples on glass bottom multiwell plates (Molecular Instruments, <https://www.molecularinstruments.com/protocols>). Wells were washed 4 times with 2X SSC (Invitrogen #15557-044), pre-hybridized in probe hybridization buffer (Molecular Instruments) for 30–60 min at 37°C and hybridized overnight at 37°C with 1.2 pmol of each probe set mixture containing 400 U/mL RNase inhibitor (Enzymatics #Y9240L). Custom probe sets were designed by Molecular Instruments (see **Table S3**). After hybridization, wells were washed with probe wash buffer (Molecular Instruments) supplemented with 400 U/mL RNase inhibitor at 37°C for 30 min and washed again 4 times with 2X SSC at RT. Amplification buffer (Molecular Instruments) was added and incubated for 30–60 min at RT. During this incubation, 18 pmol of hairpin amplifiers were heated to 95°C for 90 sec, protected from light and cooled to room temperature, then combined and added to amplification buffer containing 400 U/mL RNase inhibitor. Hairpin mixtures were incubated in the appropriate wells while protected from light for 45 min at RT for single molecule and diffraction-limited amplification. Excess hairpins were removed, and wells were again washed with 2X SSC four times. Nuclei were labeled with 2 µg/mL DAPI in 2X SSC for 5 min, followed by additional washes with 2X SSC. Samples were stored protected from light at 4°C in 2X SSC with 400 U/mL RNase inhibitor until imaging. Wash volumes used were 500 µL, and all other incubation steps used 250 µL per well, added using a multi-channel pipette or P1000 in a 24-well plate format.

Cardiomyocyte imaging

All cardiomyocyte imaging in this study was performed on a 3i spinning-disk microscope with a 63x/1.2 NA W C-Apochromat Korr UV-vis IR objective (Zeiss) and a 0.83x tube lens adapter for a final magnification of 52.29x, a CSU-W1 spinning-disk head (Yokogawa) and a Prime BSI sCMOS Camera (Photometrics) (pixel size 0.124 µm in X-Y and 0.33 µm in Z). Standard laser lines (405, 488, 561, 640 nm), primary dichroic (RQFT 405, 488, 568, 647 nm) and the following Band Pass (BP) filter sets (Chroma) were used for fluorescent imaging: 450/50 nm for detection of DAPI, 525/50 nm for detection of mEGFP, 600/50 nm for detection of Alexa 546 dye and 690/50 nm for detection of Alexa 647 dye. For all live cell imaging, cells were imaged in phenol red-free RPMI-1640 (Gibco #11835030) supplemented with B27 containing insulin media, within an incubation chamber maintaining 37°C and 5%

CO₂. Brightfield images were acquired using an LED light source with peak emission of 740 nm with narrow range and a BP filter 706/95 nm for brightfield light collection.

ML-based single-cell segmentation of WGA-stained live cardiomyocytes

We developed a deep learning-based instance segmentation workflow to segment individual cardiomyocytes via the WGA channel from maximum intensity projections (MIPs) of 3D image z-stacks. The segmentation workflow includes both the results of a deep neural network model called DeepLabV3 (Chen et al., 2017) as well as several other classic image processing steps. The details of the iterations we used to train the final DeepLabV3 model that was applied to the full dataset are described below. The first step in the segmentation workflow was the application of a trained DeepLabV3 model (different versions depending on the training iteration) to the WGA MIP images to create a predicted probability map of cell boundaries. We then binarized the probability map with the empirically determined cutoff value of 0.8. Next, the binary mask of the cell boundaries was refined by morphological closing (disk structuring element of radius $r = 5$ pixels) and a morphological dilation (disk structuring element, $r = 4$ pixels). Each connected component greater than 3000 pixels, excluding cell boundary pixels, was assigned a unique integer and thus represented an individual cell. Integers were indexed sequentially, with 0 representing the background. Finally, each individual cell mask was refined once more by a morphological opening and dilation (disk structuring element, $r = 5$ pixels) and by filling any holes smaller than 1200 pixels. The resultant 61,148 cell segmentations were then manually curated to generate 18,996 cells for analysis.

The final DeepLabV3 WGA cardiomyocyte segmentation model was trained in two iterations. First, we manually traced the cell boundaries of 44 2D WGA MIP images using the paintbrush tool in FIJI (Schindelin et al., 2012). We used these annotations as the ground truth to train the first iteration of the DeepLabV3 model. We then used this model within the segmentation workflow above to process 170 additional images. We selected 63 of these images that contained segmentation errors and repaired the segmentation errors manually. This created a final set of 107 images which we used to train the second, and final, iteration of the DeepLabV3 model. Implementation of the DeepLabV3 training was streamlined by using the code base within the Allen Cell Structure Segmenter (Chen et al., 2020).

Manual cell annotations of FISH data in Napari

Manual cell annotations were performed to segment single cells in all FOVs obtained from wells used for RNA FISH studies, as they did not receive WGA-staining as described above for live cardiomyocytes. Multi-channel Z-stacks were loaded into Napari (<https://napari.org>, Napari contributors, 2019) and 2D single cell masks were generated by manually drawing cell boundaries in 2D while incorporating information from all channels collected during imaging (brightfield, two FISH probe channels, nuclei via DNA dye (DAPI), and alpha-actinin-2-mEGFP (structure)). FOVs from each alpha-actinin-2-mEGFP/FISH experiment well (structure/FISH) were randomly split into groups and each group was assigned to one of three expert human annotators for manual cell segmentation. Cell boundaries were manually drawn for cells that were mostly within the FOV, and low confidence/high cell density regions with many overlapping cells were avoided. To speed up loading time for structure/FISH images in Napari, each image was down-sampled prior to manual annotation using the scale function in ImageJ, converting each 1776 x 1736 pixels x 50 planes Z-stack to an 888 x 866 pixels X 35 plane Z-stack using bilinear average interpolation. The 2D single cell masks were then rescaled to their original size prior to RNA FISH probe quantification. 2D single cell masks were used downstream to create single cell transcript abundance measurements, manual annotations of cell organization, single cell organizational scores, and integrated transcript abundance and organizational analysis in single cells (see “RNA spot segmentation and feature extraction”, “Expert annotation of cell organization”, “ML-based alpha-actinin-2 pattern classification”, and “FISH and alpha-actinin-2 assay data preparation” sections in STAR methods).

DNA (Nuclear) segmentation in FISH samples

Nuclear segmentation in 2D using the DNA channel was performed using CellProfiler (version 3.1.8, McQuin et al., 2018) for all FISH data sets. See CellProfiler pipeline included in the corresponding GitHub repository for details (Kamentsky et al., 2011). The DNA channel maximum intensity projection (MIP) was normalized with CellProfiler’s RescaleIntensity module from the 5th percentile to 95th percentile of the raw image. Nuclei were segmented using minimum cross entropy thresholding to define the probability distributions of foreground and background regions in an image using CellProfiler’s IdentifyPrimaryObjects module. Clumped objects were filtered by shape to identify nuclear objects in close proximity to each other. Objects smaller than 5,000 pixels were considered debris and discarded. Nuclei were assigned to a cell if their centroids fell within the 2D segmented cell object. Unassigned nuclear objects were discarded and not used for further analysis.

RNA spot segmentation and feature extraction in FISH samples

Channels with labelled RNA FISH transcripts were segmented using the Allen Cell Structure Segmenter (Allen Institute for Cell Science, 2020; Chen et al., 2020) by creating a transcript-specific segmentation workflow for the maximum intensity projection (MIP) RNA FISH images. MIP image intensities were normalized to fall between 3 standard deviations below the mean image intensity and 18 standard deviations above the mean intensity, and a Gaussian smoothing filter was applied to the images. A 2D spot filter algorithm was applied to the normalized images to segment the transcript signal. Each transcript signal was assumed to represent the location of the RNA species as a diffraction-limited spot. This filter considers both the radius of the dots and the filter response to generate the binary results. After visual inspection of images, we estimated the dot diameter to be 1-2 pixels and thus set the default

value of the dot radius parameter to 1. Dot intensity levels varied by transcript; thus, filter response parameter values were individually optimized for each RNA species to account for this variation as shown in the table below (probe set is indicated by gene name and corresponding amplifier wavelength). The gene *TTN* is included in the table below and data package but is not shown in [results](#). Segmented RNA FISH spots were quantified for each manually segmented cell in an FOV using CellProfiler's IdentifyPrimaryObjects and MeasureObjectSizeShape modules.

Microscope	Probe set	Filter response parameter
3i	<i>COL2A1</i> -638	0.03
	<i>MYH7</i> -638	0.02
	<i>BAG3</i> -638	0.04
	<i>H19</i> -638	0.02
	<i>HPRT1</i> -561	0.05
	<i>MYH6</i> -561	0.04
	<i>TCAP</i> -561	0.02
	<i>ATP2A2</i> -561	0.01
	<i>TTN</i> -561	0.01
	<i>TTN</i> -638	0.01
	<i>ACTN2</i> -561	0.02
	<i>ACTN2</i> -638	0.02
	<i>PLN</i> -561	0.01
	<i>MYL7</i> -647	0.01
	<i>MEF2C</i> -561	0.03
	<i>NKX2-5</i> -561	0.01
	<i>BMPER</i> -561	0.04
	<i>CNTN5</i> -638	0.04
	<i>VCAN</i> -638	0.04
	<i>PRSS35</i> -638	0.02

Expert annotation of cell organization

Two experts manually scored each segmented cell for its overall alpha-actinin-2 organization. Each expert was presented with single cells cropped from a FOV (after manual annotation of single cell masks, see “[Manual cell annotations in Napari](#)” section for details); all cells were scored twice, once by each expert. Cells were scored as falling into one of five categories from 1–5; [Figure 2A](#) shows a schematic of the patterns that are representative for each class. Cells assigned a score of 1 had sparse, randomly organized puncta; cells assigned a score of 2 had denser puncta that were more organized; cells assigned a score of 3 exhibited a mix of puncta and other structures, including fibers and z-disks; cells assigned a score of 4 exhibited predominantly regular z-disks without a single clear axis of alignment; and cells assigned a score of 5 exhibited almost exclusively regular z-disks with a clear axis of alignment. Experts made their score based on the majority of the cell’s organization falling into one of these five categories. For example, a cell that had predominantly regular z-disks, but some puncta and fibers would still be categorized as a 4. Cells with approximately half regular structures and half irregular structures were nearly always categorized as a 3 (see [Figure S2I](#)). After all cells in the data set had been scored by both experts, annotations that differed by more than two units were curated; in general, these differences reflected cells with very low intensity alpha-actinin-2 signal. In these cases, experts established concordance after review. A total of 5,161 cells were scored in the original training set (4,823 after filtering; see “[Linear model predicting expert organization scores from single cell metrics](#)” section below, [Figures 5A–5C](#) and [S4A–S4C](#)), and an additional 1,000 cells for each of the two test sets (932 cells for test set 1 and 922 cells for test set 2 after filtering out the dimmest 5% of cells, based on total alpha-actinin-2 intensity, see “[Alpha-actinin-2 intensity measurements](#)” section below; [Figure 5A](#)). Within the FISH data sets, cells that did not show any alpha-actinin-2 mEGFP protein expression were scored a “0,” and these cells were removed from downstream analysis. This represented 832 of 13,773 cells, which aligns with the GFP-negative cell population shown by flow cytometry analysis in [Figures S1D](#) and [S1E](#) and [Table S1](#).

ML-based alpha-actinin-2 pattern classification

A machine learning (ML) based alpha-actinin-2 pattern classifier was created based on images of live replated cardiomyocytes imaged on a 3i spinning disk microscope as described above in the “[Imaging replated cardiomyocytes](#)” section. This classifier

was then validated for use in images of fixed alpha-actinin-2 images of the type used in this study (Figures S2A and S2B). An expert manually annotated 3589 regions of 18 representative z-stacks of alpha-actinin-2-mEGFP into five classes according to their alpha-actinin-2 pattern: diffuse/messy, fibers, disorganized puncta, organized puncta, and organized z-disks. Fibers correspond to elongated thread-like patterns; diffuse/messy regions captured areas with many overlapping patterns or lacking discernible organization; disorganized puncta were assigned to small punctate structures with no obvious orientation; organized puncta were used to categorize regions with punctate structures that were organized along a discernible axis; and organized z-disks were used to capture well-aligned, stripe-like structures. We used Napari (<https://napari.org>, Napari contributors, 2019) to click on and annotate pixel-based regions for each class; only the slice with the highest average intensity was used for manual annotation. We looked for regions in each image that clearly corresponded to each pattern category and captured the variation in these patterns. While we captured over 500 annotations for each pattern class, we did not fully annotate all regions of any image in the training set. Representative examples of these classes are shown in Figures 2A–C and S2A; this annotation was meant to capture the variety of patterns observed in the data set.

To identify background regions, we used the filament3d Jupyter notebook workflow template from the Allen Cell Structure Segmentationer to segment the images in 3D (Chen et al., 2020), and then converted the 3D stack into a 2D image by keeping only the slice with the highest average intensity. Next, we tiled the image with tiles of size 64x64 pixels and computed the total number of foreground pixels inside each tile; tiles with less than 64 foreground pixels were flagged for the next step. We calculated the distance between every pixel in the flagged tiles to the closest foreground pixel. If that distance was greater than 64, we classified that pixel as background.

Each non-background annotation was stored as an (X, Y) coordinate and used as training data for a deep-learning-based classifier model. Training data was drawn from live cell imaging of replated alpha-actinin-2-mEGFP (AICS-0075 ACTN2-mEGFP) cardiomyocytes. This data was split into train/test data sets, with 80% of the data being used for training and 20% held out as a testing set. We used a ResNet18 convolutional neural network pre-trained on the ImageNet data set as our classifier. All layers of this network were fine-tuned, and the last layer was trained from scratch on our training set. We used patches of 96 x 96 pixels centered around each annotation, upsampled to 256 x 256 pixels through linear interpolation, as input to the network. The network was trained to predict the class of the center pixel of the patch. We trained the model for 750 epochs and we applied the trained model to the test set, where the model performed with 83% accuracy (see Figure S2C). We used a separate data set of alpha-actinin-2-mEGFP cardiomyocytes that was imaged both in live and fixed conditions to determine how the fixation process impacts the classifier performance. Because the alpha-actinin-2 signal from live cell imaging was brighter than the signal in the matched fixed images, the histograms of the fixed images were matched to the average histogram of the live cell training data set prior to applying the model. Figures S2A and S2B shows that there are only minor changes in the overall prediction suggesting that the fixation process has negligible impact for use of this model. The intensities for the FISH data set were not normalized to live cell imaging intensities as their signal was adequate for classifier performance. The ML model was used to make pixel-wise predictions of the alpha-actinin-2-mEGFP pattern classes on the highest intensity slice of all fields of views used in this paper. For these predictions, each image patch was evaluated by the model 4 times: once in an unaltered state, and three times with the patch undergoing randomized mirroring and rotation. The class probabilities from each round were averaged together for the final classification. The resulting classification maps were masked based on the single cell masks (see “[Manual cell annotations in Napari](#)” section) to calculate and output the fraction of cell area covered by each alpha-actinin-2-mEGFP pattern class on a per cell basis.

Quantification of global sarcomere alignment

To quantify global structural alignment, we implemented a method described in (Sutcliffe et al., 2018) which uses the correlation of a gray-level co-occurrence matrix to quantify patterns of sarcomeric organization. In this approach, the element (i,j) of the co-occurrence matrix of an image I of dimension $N \times M$ is defined as

$$C_{d,\theta}(i,j) = \sum_{x=1}^N \sum_{y=1}^M 1, \quad \text{if } I(x,y)=i \text{ and } I(x+d,y+\theta)=j, \text{ or } 0 \text{ otherwise,}$$

and it represents the number of times that grey-level j occurs at an offset distance d and at an angle θ from grey-level i . The correlation of the co-occurrence matrix measures the joint probability of pairs of gray-levels and it is defined as

$$\text{Corr}_{d,\theta} = \sum_{ij=0}^{\text{levels}-1} C_{d,\theta}(i,j) \left[\frac{(i - \mu_i)(j - \mu_j)}{\sqrt{\sigma_i^2 \sigma_j^2}} \right].$$

The correlation function displays a fast exponential-type decay in cells with no regular patterns. The correlation function oscillates when regular patterns with no preferential direction of alignment are present (see Figure 3Bii). A mix of exponential-decay and oscillatory behavior is observed in cases where a preferential direction of alignment is present (Figure 3Biii). In (Sutcliffe et al., 2018) the authors suggest using the height of the highest peak as a score for sarcomere organization. To detect the highest peak, we first fit the exponential decay component of the correlation curves as shown by the dashed lines in Figures 3Bi–3Biii. Next, we subtracted the fitting curves from the raw data to produce the curves shown in Figures 3Ci–3Ciii. The height of the highest peak is easily identified in the curves and shown by the horizontal dashed line, and green arrow labeled “peak height”. The offset distance for which the highest

peak occurs, identified by the vertical dashed line, and green arrow labeled "peak distance", was used as a metric for sarcomere spacing.

We also used the maximum coefficient of variation of the correlation signatures as a metric for global sarcomere alignment. This metric is particularly useful for distinguishing between aligned and non-aligned fibers. In the case of well aligned fibers, we see heterogeneity in the Haralick decay profiles, while for poorly aligned fibers, the decay profiles are homogeneous. This difference is effectively captured by the coefficient of variation, even though the curves lack a clear peak. The maximum coefficient of variation is defined as:

$$cv = \max_d \left(\frac{\sigma_d}{\mu_d} \right), d \in \{1 \dots N_d\}.$$

The mean response μ_d for a given distance d is defined as

$$\mu_d = \varepsilon + \frac{1 - \varepsilon}{N_0} \sum_{i=1}^{N_0} |\text{Corr}_{d,i}|,$$

and the standard deviation is given by

$$\sigma_d = \sqrt{\frac{1}{N_0 - 1} \sum_{i=1}^{N_0} |\text{Corr}_{d,i} - \mu_d|^2}.$$

The variable ε is a numeric regularization factor chosen to be 0.1. The total number of values of d was = 32 and the total number of different angles was = 16 for all experiments. Prior to co-occurrence matrix calculation, every cell image was converted to 3-bit format (*levels* = 8) with the same number of pixels in each level. Background was not included in the co-occurrence matrix calculation.

ALPHA-ACTININ-2 INTENSITY MEASUREMENTS

Measurements of alpha-actinin-2 intensity were made by sum projecting a 3D image stack to capture all alpha-actinin-2-mEGFP signal in the image stack. Raw and background-subtracted sum projections were calculated for each cell in the live datasets (Experiments 1-7 are outlined in [Table S1](#)) and a subset of fixed experiments in which ACNT2 transcript levels were also probed (Experiments 1, 6 and 7, D25 timepoints). The background intensity was defined as the first percentile of the image intensity distribution for all slices across a 3D image stack. For all plots related to alpha-actinin-2-mEGFP protein intensity, measurements are reported as effective protein density, or intensity units per 2D projected cell area. Live data was segmented using an automated segmentation algorithm based only on WGA and nuclear staining. Due to the presence of alpha-actinin-2-mEGFP negative cells in our cardiac populations ([Figures S1D and S1E; Table S1](#)), the lowest 5% of cells were filtered out.

FISH AND ALPHA-ACTININ-2 ASSAY DATA PREPARATION

For all analysis of the relationship between transcript abundance (RNA FISH) and alpha-actinin-2 structural organization, we used a data set of 1,215 five-channel 3D FOVs from D18 and D32, projected into 2D by calculating the maximum intensity along the z-axis. From these 2D fields, we manually segmented 12,941 single cell masks using Napari (see "[Manual cell annotations in Napari](#)"). For each single cell mask, we then had five channels of data: two RNA FISH probe channels, one channel of fluorescently tagged alpha-actinin-2 protein, a brightfield channel, and a fluorescent nuclear dye channel (DAPI). Additionally, we assayed two FISH probes at D25: ACTN2 and TTN (n = 1,031 cells across 3 independent experiments; TTN analysis is not included in [results](#), but is included in the data package), and eight pairs of FISH probes at D18 and D32: HPRT1 and COL2A1 (n = 717 cells at D18, n = 487 cells at D32), MYH6 and MYH7 (n = 719 cells at D18, n = 578 cells at D32), TCAP and BAG3 (n = 639 cells at D18, n = 522 cells at D32), ATP2A2 and H19 (n = 639 cells at D18, n = 522 cells at D32), NKX2-5 and CNTN5 (n = 813 cells at D18, n = 750 cells at D32), MEF2C and MYL7 (n = 896 cells at D18, n = 645 cells at D32), PLN and PRSS35 (n = 902 cells at D18, n = 672 cells at D32), and BMPER and VCAN (n = 868 cells at D18, n = 766 cells at D32). All other channels were identical throughout the experiment. All D18 and D32 FISH data was generated from one of two independent experiments, where each probe was assayed once across two replicate wells. In addition to the raw image channels, segmentations were performed for all channels other than the brightfield. Both the raw and normalized 2D images and segmentations are available in the data supplement.

From these five channel images, we constructed a variety of quantitative metrics, which are available in tabular form in the supplemental data. The quantitative metrics fall into four categories:

1. Cell features: the segmented images were processed by CellProfiler to generate cell area and aspect ratio measurements for each cell. An exhaustive list of single cell features was generated and is included in the corresponding quilt data package.
2. Expert scores of sarcomeric organization: the structural maturity of the cells was assessed by two human experts, on an ordinal scale of 1–5. See "[Expert annotation of cell organization](#)" section.

3. Local organization: all pixels in individual cells were classified according to their alpha-actinin-2 pattern: diffuse/messy, fibers, disorganized puncta, organized puncta organized z-disks or background. These scores were aggregated at a single cell level as six numbers that represent the fraction of the cell area covered by each of these classes. See “ML-based alpha-actinin-2 pattern classification” section.
4. Global alignment: three metrics for global sarcomere alignment was calculated for each cell. See “quantification of global sarcomere alignment” section.

We focus on a subset of 11 simple features for our modeling: two features that describe the cell’s gross morphology (cell area and cell aspect ratio), six features that describe the cell’s local structure (described in the “ML-based ACTN2 pattern classification” section), and three features describing the cell’s global sarcomeric alignment (described in the “quantification of global sarcomere alignment” section; Figure 4 step C).

All data used to generate figures in this manuscript, including the 30,986 total single cells included in these analyses, is available at: https://open.quiltdata.com/b/allencell/packages/aics/integrated_transcriptomics_structural_organization_hipsc_cm

Linear model predicting expert organization scores from single cell metrics

The combined organizational score used for further analysis in Figures 4 and 5 was constructed using ordinary least squares regression, using the eleven cell features in Figure 4 step C to predict the human expert annotation scores, which are integer values from one to five. In order to maintain predictive fidelity to biologically important but low abundance extremal scores, the regression was fit using sample weights in inverse proportion to the abundance of the sample’s expert annotation score. The regression also included a minute ridge penalty for numerical stability. All features were standardized to zero mean and unit variance before fitting the model, in order to more reasonably assess relative importance of the features using the coefficients of the fitted model. Lastly, an offset term was calculated for the regression. Final calculated feature weights and 95 percent confidence intervals are listed in Table S2. All details are available in our GitHub repository (https://github.com/AllenCellModeling/fish_morphology_code).

Once fit to the entire training data set of 4,823 cells, the model was then applied to the data set to generate the combined organizational score for each cell as a linear combination of the input features, using the regression coefficients (and offset) of the linear model as weights. This regression model was then applied to two independent datasets without refitting. In each of these test data sets 1,000 cells were manually scored by two experts which verified a good model performance in these independent datasets (Figure 5A). Because the number of features is so small compared to the number of data points, overfitting concerns are minimal.

Bootstrapped confidence intervals

Confidence intervals are calculated using bootstrap resampling (Efron, 1979; Wasserman, 2006). The data set is resampled (with replacement) 1,000 times, and the statistical operation of interest (Spearman correlation, linear regression, etc.) is computed on each bootstrap sample. The values for that statistic are then ranked, and the values at the 2.5 and 97.5 percentiles are reported as the lower and upper bounds of the 95% confidence interval (Tables S2 and S4). Bootstrapped statistics are displayed in box and whisker plots (Figures 4F, 6B, S5A, S6G, S7A, S7C, S7D, and S7E) with outliers defined as being outside 1.5 times the interquartile range (IQR).

Probability densities

The marginal density histograms in Figures 5B–5D, S4A, S4B, S5D, and S6F’ are normalized such that the area under each curve integrates to one, i.e., they are probability densities.

Correlation analysis

For variables that are either ordinal or continuous, correlations are assessed via Spearman rank-correlation (Spearman, 2010), a robust correlation estimator that quantifies the monotonicity of the relationship between two variables. We treated our time point data as a binary categorical variable rather than as an ordinal variable; thus, differences between other continuous and ordinal variables as a function of day were assessed using a Mann-Whitney U-test (Mann and Whitney, 1947). This test is a non-parametric quantification of how likely it is that samples were drawn from the same distribution. Data tabulation and statistical calculations were performed in Python 3.7 using the Numpy 1.18.2, Scipy 1.4.1, Pandas 1.0.3, scikit-learn 0.22.2, AnnData 0.7.1, and Pingouin 0.3.3 libraries. Plotting was performed using the Altair 4.0.1 and Seaborn 0.10.0 visualization libraries (McKinney, 2010; Oliphant, 2006; Pedregosa et al., 2011; Vallat, 2018; Van Rossum and Drake, 2009; VanderPlas et al., 2018; Virtanen et al., 2020; Waskom et al., 2020; Wolf et al., 2018). Data organization and distribution was performed using quilt3distribute 0.1.3 (Brown, 2019).

Differential expression between MYH6 and MYH7

In the subset of cells ($n = 1,297$) where MYH6 and MYH7 were jointly probed via RNA FISH, an aggregate per-cell score was constructed to indicate the relative expression of MYH6 vs MYH7, shown in Figure S5D. First, the segmented FISH spot counts for each gene in each cell (see “RNA spot segmentation and feature extraction” section) were normalized by the cell area to create a count density for each gene in each cell: $d_i^g = c_i^g/a_i$ where c_i^g is the count of gene g in cell i , a_i is the area of cell i , and d_i^g is the density of gene g in cell i . Densities of each gene were then normalized by the median expression of each gene to account for the different scales of their respective expression densities, creating a normalized density metric: $n_i^g = d_i^g/M_g$ where $M_g = \text{Median}_i(d_i^g)$ is the median expression

density of gene g over all cells i in which it was probed. The relative expression density of *MYH7* to *MYH6* in each cell is then calculated as $r_i = (n_i^{\text{MYH7}} - n_i^{\text{MYH6}}) / (n_i^{\text{MYH7}} + n_i^{\text{MYH6}})$.

QUANTIFICATION AND STATISTICAL ANALYSIS

Details of specific statistical analyses for each section, sample sizes, and statistical tests used are given in the [STAR methods](#) and in the corresponding figure legends.